Materials Science & Engineering A 959 (2026) 150024

Contents lists available at ScienceDirect

Materials Science & Engineering A

journal homepage: www.elsevier.com/locate/msea

The role of martensite decomposition and β-stabilizer segregation to interfaces in Ti-6Al-4V with an initial dual-phase α+α' microstructure

N. Pfeffer [a,*], A. Bezold [a,b], J. Vollhüter [a], O. Nagel [a], M. Weiser [a], A. Stark [c], S. Neumeier [a], H.W. Höppel [a]

[a] Friedrich-Alexander-Universität Erlangen-Nürnberg (FAU), Department of Materials Science & Engineering, Institute I: General Materials Properties, Martensstraße 5, 91058, Erlangen, Germany
[b] Now at: the Ohio State University, Department of Materials Science and Engineering, 140W 19th Ave., Columbus, OH, 43210, USA
[c] Helmholtz-Zentrum Hereon, Max-Planck-Straße 1, 21502, Geesthacht, Germany

ARTICLE INFO

Keywords:
Ti-6Al-4V
Short-time heat treatments
Martensite decomposition
V-/Fe-rich nano-scale clustering
Lattice relaxation
High resolution microstructural analysis
Strengthening
Titanium alloys
High resolution electron microscopy (HREM)
Atom probe tomography (APT)
High energy X-ray diffraction (HEXRD)

ABSTRACT

The strength of dual-phase α+α' Ti-6Al-4V sheet material can be significantly enhanced through additional short-time annealing lasting only a few minutes, as shown in previous work and attributed to nano-scale microstructural changes within the martensitically transformed β-phase. However, the microstructural mechanisms remained unclear. In this study, the microstructures of the as-received state, the solution heat treated state with α+α' microstructure and additionally (short-time) annealed states were compared to provide deeper insight into these microstructural processes. Advanced high-resolution techniques, including high resolution scanning transmission electron microscopy, atom probe tomography and high-energy X-ray diffraction, were combined with tensile testing for mechanical assessment. Short-time annealing of metastable Ti-6Al-4V α+α' microstructures at 570 °C for 180 s triggered an α' → α+β transformation, comprising: (i) chemical changes, involving V- and Fe-segregation to interfaces, and the formation of V-/Fe-enriched clusters; and (ii) crystallographic decomposition, manifested by α' lattice relaxation and lattice parameter changes. With prolonged annealing, element partitioning and β precipitation progressed from the clusters and nuclei located along interfaces, accompanied by slight changes in the lattice parameters of both phases. After 3 h, the microstructure approached equilibrium, with stabilized α and β phase fractions and lattice parameters. The strengthening achieved by short-time annealing is attributed to suppression of reorientation-induced plasticity in prior α'-martensite and dislocation-cluster/precipitate/solute interactions. In summary, this work reveals microstructural evolution and processes during martensite decomposition in dual-phase Ti-6Al-4V, including β-stabilizer segregation to interfaces. Further, it discusses their role in strength enhancement, providing guidance for developing effective heat treatment and processing routes.

1. Introduction

The most efficient utilization of the material potential for high-performance applications is of fundamental technological interest. One approach involves the implementation of novel heat treatments or thermo-mechanical strategies on alloys for the purpose of specifically modifying the microstructure and thereby improving properties. A multitude of examples can be found in literature for several different alloy systems, including titanium alloys [1–6].

A variety of microstructures and mechanical properties can be obtained in α+β titanium alloys through thermal or thermomechanical treatments [7,8]. Owing to the presence of both α- and β-stabilizing elements, the α+β two-phase region – in which the low temperature hexagonal close packed (hcp) α-phase and the high temperature body centered cubic (bcc) β-phase coexist – extends to relatively high temperatures. In Ti-6Al-4V, aluminum (Al) serves as a stabilizer of the hcp α-phase, while vanadium (V) and iron (Fe) act as stabilizers of the bcc β-phase. The standard orientation relationship between the bcc β-phase and the hcp α-phase follows the Burgers relationship characterized by $\{0001\}_\alpha \,||\, \{110\}_\beta$ and $\langle 11\text{-}20\rangle_\alpha \,||\, \langle 111\rangle_\beta$ [9–12].

It is further well established that certain titanium alloys, including Ti-6Al-4V, can undergo a displacive martensitic transformation from the parent β-phase if the cooling rate exceeds a critical threshold and diffusional transformations are suppressed [13–17]. Depending on the concentration of β-stabilizing elements present in the prior β-phase, the resulting metastable martensitic phase may adopt either a distorted hcp (α')

* Corresponding author.
E-mail address: nina.pfeffer@fau.de (N. Pfeffer).

https://doi.org/10.1016/j.msea.2026.150024
Received 7 November 2025; Received in revised form 13 February 2026; Accepted 2 March 2026
Available online 3 March 2026

or a more severely distorted orthorhombic (α") lattice structure [18,19].

Solution heat treatment in the α+β two-phase region just below the β transus temperature (T_β) followed by water-quenching can produce microstructures consisting of primary α-grains and fully-martensitic transformed prior β-grains. Such α+α' or α+α" dual-phase microstructures in titanium alloys can exhibit a high work-hardening potential combined with a satisfying ductility [20–25]. These properties are commonly attributed to the composite-like behavior arising from the different mechanical behavior of the two phases, as well as to specific deformation mechanisms such as the reorientation induced plasticity (RIP) effect. When considering Ti-6Al-4V, quenching from the upper α+β region leads to a β → α' transformation, resulting in α+α' microstructures [25,26]. The mechanisms of RIP in such Ti-6Al-4V α+α' microstructures has been described by O. Dumas et al. [26,27]. It involves the reorientation of certain α'-plates under uniaxial loading, facilitated by the mobility of the {13-41} α' twin planes that occur between different α'-variants within a self-accommodating plate group. The appearance and the extent of the RIP-effect depend on several factors, including the chemical composition of the martensite, the interaction energy between α'-variants within one prior β-grain, and the crystallographic orientation of the parent β-grain relative to the loading direction.

While the combination of enhanced work-hardening capacity and high ductility can be advantageous for certain applications of titanium alloy, the metastable nature of the martensitic α'-phase presents a technological limitation, as it tends to evolve toward thermodynamic equilibrium. Previous investigations by N. Pfeffer et al. demonstrated that Ti-6Al-4V sheet material – solution heat treated in the upper α+β region, water-quenched, and thus exhibiting an α+α' microstructure – can attain a substantial increase in strength after a very brief annealing treatment [25,28]. This finding highlights new technological opportunities, particularly for sheet materials and the fabrication of thin-walled sheet metal components with superior strength [28]. Other researchers have consistently reported an increase in strength of Ti-6Al-4V after short-time annealing of a short-time solution heat treated and quenched (STQ) condition [29–31]. However, the mechanisms by which the strength is increased after short annealing times have not yet been conclusively clarified.

T. Morita et al. [29] and S. Tanaka et al. [30] reported in their studies on Ti-6Al-4V, that the STQ treatment (930 °C, 120 s, WQ) did not completely transform the previous β-grains into martensite. Instead, a metastable β-phase was found to remain, in which finely distributed α-phase was proposed to precipitate besides stable β-phase during the subsequent short-time annealing. They attributed the strengthening by annealing to the α-precipitate-formation. P.J. Fopiano and C.F. Hickey [31] reported a rapid initial increase in hardness during annealing when starting from α+α' microstructures without retained metastable β-phase, ascribing it to the decomposition of martensite. However, the methods they applied did not provide an adequate resolution of microstructural events and element distributions after short annealing times due to their inherent fine-scale nature. In earlier work by N. Pfeffer et al. [25], high energy X-ray diffraction (HEXRD) results were interpreted as evidence for the onset of martensite decomposition when comparing the STQ-state to the additionally short-time annealed state. However, none of these publications provides a detailed account of the underlying microstructural processes or a thorough analysis of how they relate to the resulting mechanical properties.

To date, extensive research on the (initial) microstructural evolution during martensite decomposition in titanium alloys has primarily focused on alloys processed through laser powder bed fusion (LPBF), as for example in Refs. [32–35]. In SEM observations, as-built LPBF microstructures of Ti-6Al-4V typically appear fully-martensitic, which is the result of high cooling rates occurring in the deposited layers. However, several studies using techniques with higher resolution have revealed the presence of fine-scale V- and/or Fe-rich clusters in the as-built condition [32–34]. The formation of these clusters has been attributed to the repeated thermo-kinetic cycles within a layer during the deposition of additional layers, which are characteristic of the LPBF process. In this context, the phrase "martensite decomposition" has to be understood not only in terms of crystallographic changes but also incorporating diffusion processes leading to the cluster formation. J. Haubrich et al. [33] and H. Wang et al. [34] further investigated the impact of post-LPBF heat treatments and reported progressive martensite decomposition towards the thermodynamic equilibrium (α' → α+β). Both studies describe the V/(Fe)-rich clusters located at defects in the as-built microstructure to act as precursors for β-phase formation during this decomposition process. Within post-LPBF heat treatments, the applied parameters are known to play a critical role in shaping the resulting microstructural features, such as the width and aspect ratio of α-lamellae as well as the morphology and distribution of the β-phase within the (near-)equilibrium α+β microstructure, and thereby exert a strong influence on the mechanical properties [33,35–39]. Compared to the as-built Ti-6Al-4V LPBF state, which demonstrates high strength and low ductility, typical post-process heat treatments (temperatures: >700 °C; duration: in the range of few hours) reduce strength and enhance ductility - a trend that becomes more pronounced with increasing heat treatment temperature due to coarsening of microstructural features [33,36,37,39]. On the other hand, lower annealing temperatures (approx. < 600 °C) can help maintain or even increase the strength of the as-built material; however, internal stresses may not be sufficiently relieved when heat treatment times are kept in the range of few hours [33,35,40].

Returning to the context of α+α' dual-phase microstructures and the effect of annealing, it is relevant to consider the recent work by O. Dumas et al. [41]. The researchers demonstrated by electron backscatter diffraction analyses that the RIP-effect, which is manifested during deformation of STQ α+α' microstructures in the α'-phase, is suppressed after annealing for durations ≥15 min. The suppression was attributed to the presence of β-precipitates at α'/α' interfaces resulting from martensite decomposition. These precipitates were assumed to exert a pinning effect. Additionally, a chemical alteration of the former martensite during decomposition was considered likely, which would cause the critical content of β-stabilizers to fall below the level required for RIP. A suppression of the RIP-effect may also be applicable to shorter annealing times, potentially contributing to the increase in strength compared to the STQ α+α'-state, as the latter has been reported in the aforementioned literature [25,28–31].

Overall, existing studies do not yet provide a coherent microstructural explanation for the strength increase observed upon (short-time) annealing of α+α' microstructures. The aim of this study was therefore to gain deeper insight into the nanoscale microstructural processes occurring during short-time annealing of α+α' microstructures that are responsible for this strengthening effect. For this purpose, STQ material in the as-quenched condition and after additional short-time annealing was investigated and systematically compared. The heat treatment parameters were derived from previous studies and preliminary experiments and are described in detail in Section 2.2. High-resolution characterization methods were employed, including high-resolution scanning transmission electron microscopy, atom probe tomography, and high-energy X-ray diffraction. To further advance understanding, additional microstructural investigations were performed on the as-received starting material (rolled and mill-annealed condition) as well as on samples subjected to prolonged annealing. Tensile tests were conducted on selected material states to correlate microstructural features with mechanical properties.

2. Material and experimental methods

2.1. Initial material

The starting material was a 1 mm thick sheet of Ti-6Al-4V Grade 5, which underwent a rolling and mill annealing process. This material was supplied by *Shaanxi Lasting Titanium Industry Co., Ltd.* and used in its as-received (AR) condition. The chemical composition, as specified in the manufacturer's certificate, is shown in Table 1, together with own-

Table 1
Chemical composition (wt.-%) of the as-received Ti-6Al-4V sheet metal as specified in the manufacturer's certificate, together with the measured composition obtained by OES and CGHE methods.

	Ti	Al	V	O	Fe	C	Others
Certificate	Bal.	6.0	4.00-4.10	0.14-0.15	0.12-0.13	0.01-0.02	<0.01
Measured	Bal.	6.04	4.19	0.15	0.13	0.04	<0.015

measured values. The latter were obtained by optical emission spectrometry (OES), and by carrier gas hot extraction (CGHE) for oxygen. Both sets are consistent with the AMS 4911 specifications.

2.2. Production of STQ and STA material states using a vertical furnace

The selection of heat treatment parameters was guided by available literature [22,23,25,29,30,42] and further supported by preliminary experiments. A solution heat treatment temperature of 915 °C was chosen, as it provides approximately balanced volume fractions of primary α and transformed β and has been shown to yield high uniform elongation and pronounced strain-hardening capability [25]. Preliminary screening experiments were conducted to define suitable annealing parameters. An annealing temperature of 570 °C was identified as appropriate to induce a pronounced strengthening response already at short annealing times, while enabling the consideration of different microstructural mechanisms that may become relevant to the mechanical properties with increasing annealing duration.

Heat treatments were conducted in a modified vertical furnace *ROC 105/610/15* from *Thermconcept*, as previously described in detail [25]. A *Kanthal® A* wire basket was equipped with four microstructural and four tensile specimens for each treatment. Once the furnace reached the target temperature, an argon gas flow (purity grade 4.6, 99.996 %) was initiated. After a 15-min homogenization period, the basket was pre-heated above the furnace lid for 60 s, then moved to the constant temperature zone, where the temperature was controlled and monitored by a nearby thermocouple.

In this work, the STQ heat treatment parameters remained unaltered, consisting of a solution heat treatment at 915 °C (T_{ST}) for 120 s (time counted from the moment the specimen reached the constant-temperature zone), followed by water quenching, see Fig. 1 a). After pre-heating to approximately 150 °C, samples were pulled into the constant temperature zone and reached the target solution heat treatment temperature within approximately 60 s. The water quenching yielded cooling rates of approximately 300 K/s in the range between the T_{ST} to 500 °C (for the determination procedure, see [25]).

Subsequent annealing was performed at 570 °C (T_A) for various times (t_A), ranging from 180 to 21600 s (STA1-STA6), see Fig. 1 b). Samples reached around 60 °C in the lower pre-heating zone, then attained the target annealing temperature within 120 s in the constant temperature zone. After the desired annealing time was reached, the samples were air-cooled outside the furnace.

2.3. Characterization methods

Scanning electron microscopy (SEM) was used to investigate microstructural evolution across different material states on the micro- to submicron scale. The transverse direction (TD) was defined as viewing direction. For metallographic preparation, the specimens were ground to achieve parallel surfaces, fine-ground on one side, and subsequently polished with a 3 µm suspension with a force of 20 N for 10 min, followed by chemo-mechanical polishing using an OPS:H_2O_2 (9:1 ratio) suspension with 15 N for 15 min. For both polishing steps, the plate and sample holder were rotated in the same direction at identical rotational speeds. SEM analysis was performed in a *Zeiss Crossbeam 540 EsB* in backscattered electron (BSE) mode using a *Zeiss 4QBSD* detector and the following parameters: 10 kV acceleration voltage, 5 nA probe current, and at 8.5 mm working distance.

High resolution scanning transmission electron microscopy (HRSTEM) was conducted to analyze the localization of alloying elements for different material states and, in particular, to characterize the segregation of alloying elements to microstructural features during short-time annealing. Therefore, the STQ condition and the short-time annealed STA1 condition (STQ + 570 °C, 180 s, AC) were characterized and compared. For this purpose, TEM lamellae were fabricated using an *FEI Helios* 3D dual-beam focused ion beam (FIB)/SEM system. The areas of interest were protected with a Pt coating prior to milling, and FIB-based lift-outs were performed in accordance with an established protocol [43]. Standard Cu lift-out grids were utilized as support-structure for secure sample handling between the microscopes. The lamellae were shaped and thinned with a 30 kV Ga^+ ion beam. Subsequently, an ion cleaning step at 2.0 kV was employed to prevent residual sample damage. The thinning process concluded when the electron transparency became discernible as a contrast change in the secondary electron image. HRSTEM was performed on a *Thermo Fisher Scientific Spectra 200 C-FEG* microscope, equipped with a *Super-X G2* electron dispersive X-ray spectroscopy (EDS) detector and operated at 200 kV. For TEM imaging, a 30 mrad convergence semi-angle was used with collection semi-angles of 0-23 mrad for bright-field (BF) and 56-200 mrad for high-angular annular dark-field (HAADF) imaging. EDS maps were processed using *Cliff-Lorimer* analysis via *Thermo Fisher Scientific's Velox* software.

HRSTEM(-EDS) investigations were supplemented by atom probe tomography (APT) measurements to determine absolute element concentrations at interfaces. For APT tip preparation, FIB-based lift-out procedures were carried out in the *Zeiss Crossbeam 540 EsB*, following the procedure described by M.K. Miller et al. [44] and K. Thompson et al. [43]. Measurements were conducted utilizing a *Leap 4000X HR* instrument from *Cameca*, operating at a temperature of 49 K with a pulse rate of 200 kHz in laser mode with a laser energy of 50 pJ. The acquired data were processed and analyzed using *Cameca's IVAS 3.6.8* software.

Ex-situ HEXRD measurements were performed at the *P07: High Energy Materials Science beamline* at *PETRA III, DESY*, in Hamburg [45]. For this purpose, the 1 mm thick sheet metal specimens were irradiated in normal direction using an X-ray beam with an energy of 103.3 keV ($\lambda = 0.120$ Å) and a beam spot size of 1 mm × 1 mm. Diffraction signals were recorded using a flat-panel *Perkin Elmer XRD 1621* detector positioned in a distance of 1630 mm from the sample. To enhance grain statistics, the sheet specimens were additionally rotated by ± 10° around the rolling axis relative to the normal direction and the diffraction image was taken continuously during rotation. Data analysis began with a 1D reduction using the software *Pydidas* [46], calibrated with a LaB_6 standard. Subsequently, a *Rietveld refinement* was performed over a diffraction angle range of $2\theta = 2$–7° using the *FullProf* software package [47]. The instrumental broadening effect was accounted for by incorporating an instrumental resolution file, which was determined using the LaB_6 standard. The chemical phase composition constraints used for the refinement were guided by the results of HRSTEM-EDS and APT in this work, and SEM-EDS analyses reported in previous work [25]. In the as-received (AR) state, two phases were considered: the hexagonal close-packed (hcp) α-phase and the body-centered cubic (bcc) β-phase. Additionally, texture refinement for the α-phase was performed using the *March-Dollase* multi-axial model [48] for preferred orientation, specifically for (001), (101), and (110). In the STQ-state, an additional distorted hcp phase was introduced in order to distinguish α'-martensite from the α-phase. This second α' hcp phase was modeled with a different chemistry than the α-phase, as determined experimentally in [25]. Initially, the lattice and shape parameters of the α-phase were fixed,

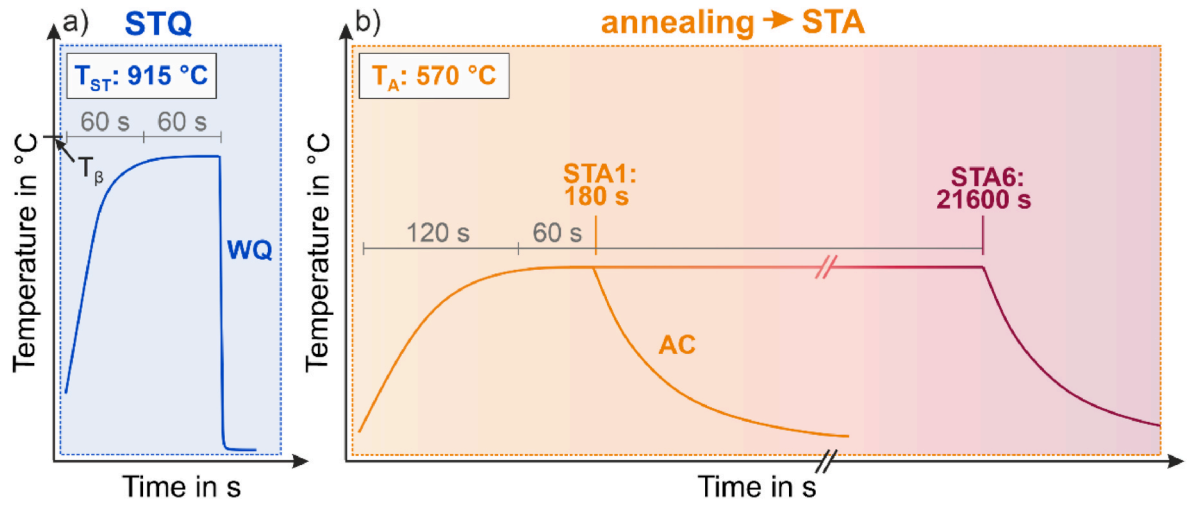

Fig. 1. Schematic temperature-time curves of the short-time heat treatments performed: a) solution heat treatment followed by water quenching (STQ) and b) additional annealing for 180-21600 s followed by air cooling resulting in the STA material state.

based on values from other material states and assuming only minor changes, while the lattice parameters *a* and *c* and shape parameters *U* and *X* of α' were refined. This yielded phase fractions in excellent agreement with experimental data from [25]. In the final refinement, the phase fractions and shape parameters of both α and α' were fixed, and their lattice parameters were released. For the STA-states, the fitting was again performed using two phases: one texture-refined hcp phase - given the challenge of clearly distinguishing between two hcp phases - and the bcc β-phase. In cases of discrepancies between the curves calculated from Rietveld refinement and measured curves, manual adjustments were applied to achieve a reasonable and accurate representation of peak details. This was particularly the case for the peaks of the β-phase present in only trace amounts, and for the STQ-state featuring two overlapping hcp phases.

Tensile testing was conducted using an *Instron 4505* universal testing machine in accordance with *DIN EN ISO 6892-1* with the following parameters: specimen geometry based on *DIN 50125/shape H*, see [25], an engineering strain rate of 10^{-3}/s, force measurement by means of a 20 kN load cell and the displacement monitored with a *laser extensometer* of the company *Fiedler Optoelektronik GmbH*. To ensure robust and statistically sound results, a minimum number of three samples per material state ($N \geq 3$) were taken into account for the evaluation of mean characteristic values. The loading direction was equal to the rolling direction.

3. Results

3.1. Microstructure of the as-received (AR) material state

The microstructure of the as-received (AR) material mainly consists of hexagonal close packed α-grains with only a small fraction of β-phase located along the α grain boundaries, see Fig. 2 a) and b). The α-grains are subject to a certain inhomogeneity in terms of morphology and dislocation density, as previously discussed in [25]. It was observed that regions containing elongated α-grains exhibit a more pronounced crystallographic texture and a higher density of small angle boundaries and dislocations compared to areas with globular α-grains. The latter is also reflected by the HRSTEM image in Fig. 2 c), where an α-grain with high dislocation density is present on the left, and a globular α-grain without dislocations on the right. HRSTEM-EDS investigations enabled a precise determination of chemical compositions of the two microstructural constituents, α-phase and β-phase and the chemical gradient across the α/β interface. Elemental maps for the elements Ti, Al, V and Fe in Fig. 2 d) represent a region containing portions of two α-grains and one β-grain. Corresponding concentration profiles are shown in Fig. 2 e). The α-phase shows an enrichment of α-stabilizer Al (~13.4 at.-%), while the β-phase is characterized by elevated levels of β-stabilizers V (~30.5 at.-%) and Fe (~2.6 at.-%). The chemical composition of the two α-grains in the AR-TEM foil were observed to exhibit slight discrepancies in terms of their Al- and Ti-content.

3.2. Microstructures of the short-time solution heat treated and quenched (STQ) and additionally short-time annealed (STA) material state

3.2.1. Comparative overview of STQ and STA microstructures from SEM and HRSTEM

By short-time solution heat treatment of the AR-material at a temperature just below the β-transus temperature, followed by water quenching, a dual-phase α+α' microstructure is achieved, as previously demonstrated in [25]. During solution heat treatment, the β-phase fraction increases due to temperature-dependent changes of phase equilibria. The hcp α'-martensite is the result of a non-diffusional displacive transformation of the prior β-phase during quenching. The solution heat treatment temperature of 915 °C employed in the present study resulted in the formation of almost equal fractions of the primary α-phase (α_p) and transformed prior β-grains (β_{trans}), as is reflected by the SEM-BSE micrographs in Fig. 2 f) and g). Due to the fast-quenching rates, a wide-range redistribution of alloying elements during quenching is effectively precluded. Consequently, the mean chemical composition of β_{trans}/α' can be considered analogous to that of the β-phase at the solution heat treatment temperature. SEM-EDS scans within α_p- and β_{trans}-grains in [25] have already proved differing mean chemical compositions of both microstructural constituents, more precisely a higher V-content and lower Al-content in β_{trans} compared to α_p. Although not shown in this work, a HRSTEM-EDS map of the area shown in Fig. 2 h) confirmed an increased content of the β-stabilizers V and Fe in the α' solid solution within β_{trans} compared to the α_p-phase, and consequently a reduced content of Ti and Al. This trend is likewise apparent in Fig. 3 b).

When comparing Fig. 2 f) and g) to i) and j), the SEM-BSE images do not uncover discernible microstructural differences between the two material states STQ and STA1. Furthermore, HRSTEM-EDS mappings revealed no significant alternations in the chemical composition of α_p- and β_{trans}-grains of the STQ- and STA1-material (not shown here).

HRSTEM micrographs in Fig. 2 h) and k) substantiate that both material states, STQ and STA1, exhibit a nearly identical structure,

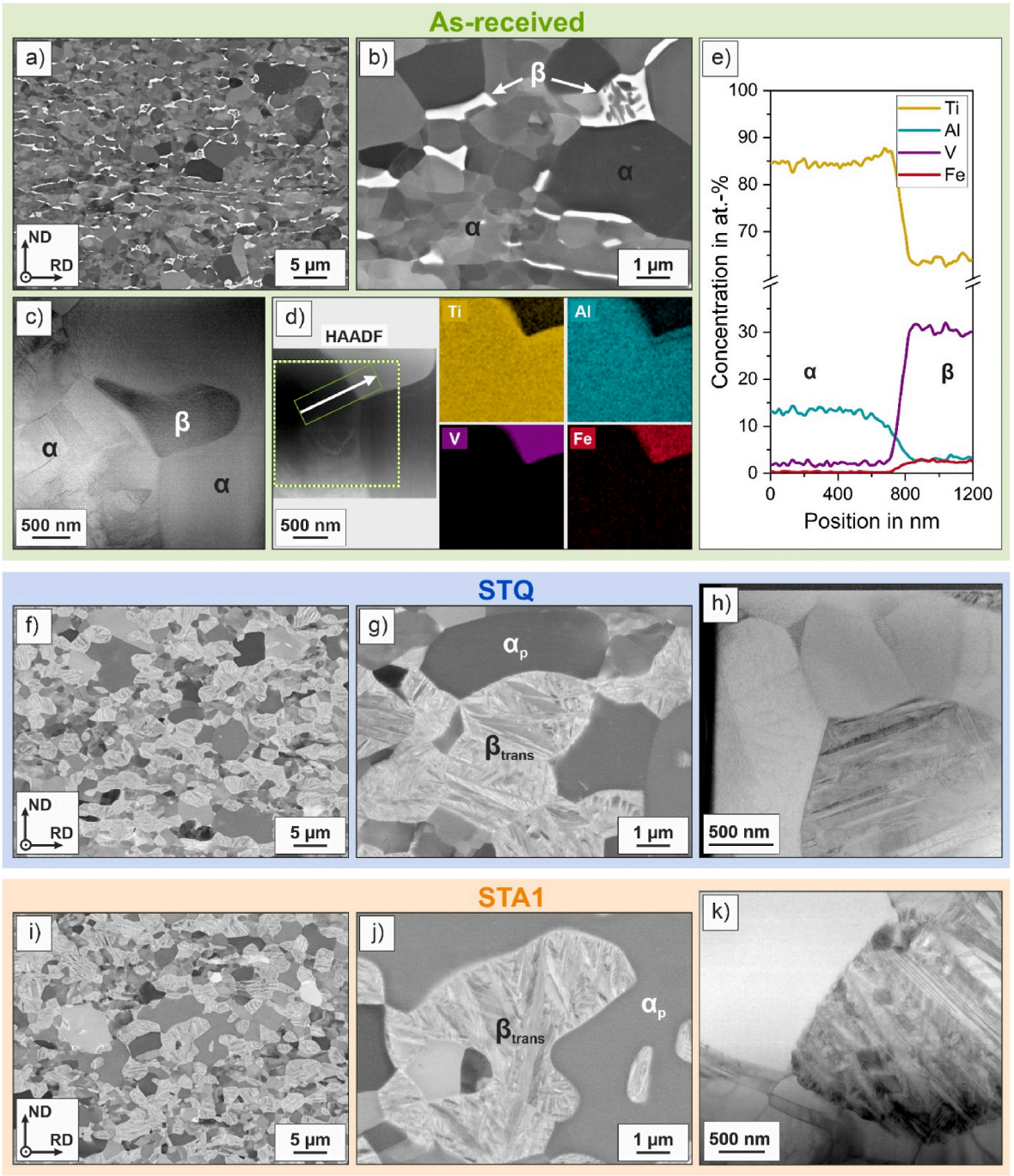

Fig. 2. Microstructural characteristics of the as-received Ti-6Al-4V sheet material represented by a) and b) SEM-BSE images, c) a HRSTEM-BF image, d) HRSTEM-EDS maps for the elements Ti, Al, V and Fe, and e) HRSTEM-EDS concentration profiles corresponding to the area marked in d). Microstructures of two heat treated Ti-6Al-4V material states: f)-h) STQ-state (915 °C, 120 s, WQ) versus i)-k) STA1-state (915 °C, 120 s, WQ + 570 °C, 180 s, AC) with SEM-BSE images in f), g) and i), j) and HRSTEM-BF overview images in h) and k).

characterized by the presence of α_p-grains alongside β_{trans} grains featuring a fine plate-like substructure, in which transformation twins are commonly observed. The latter are the result of the displacive $\beta \rightarrow \alpha'$ transformation during quenching, accommodating the lattice and shape misfit to minimize elastic stresses and achieve a more symmetric distribution of transformation strains.

Upon closer examination, in the 2D-TEM projections shown in Fig. 2 h) and k), α_p/β_{trans} interfaces appear as rather straight or uniformly curved lines in the STQ-state and as wavy lines in the STA-state.

3.2.2. Fine-scale chemical heterogeneities in STQ- and STA-material states

To further investigate interface characteristics and differences between the two material states STQ and STA1, detailed HRSTEM(-EDS) and APT investigations were performed at α_p/β_{trans} interfaces and within the fine-scale β_{trans}-microstructure. The latter includes α'/α'-interfaces and nano-twin interfaces within the α'-plates.

HRSTEM(-EDS) results for α_p/β_{trans} interfaces (STQ vs. STA1) are shown in Fig. 3, APT results in Fig. 4.

The HRSTEM images in Fig. 3 a)–d) highlight the aforementioned difference in interfacial geometry between the STQ- and the STA1-state.

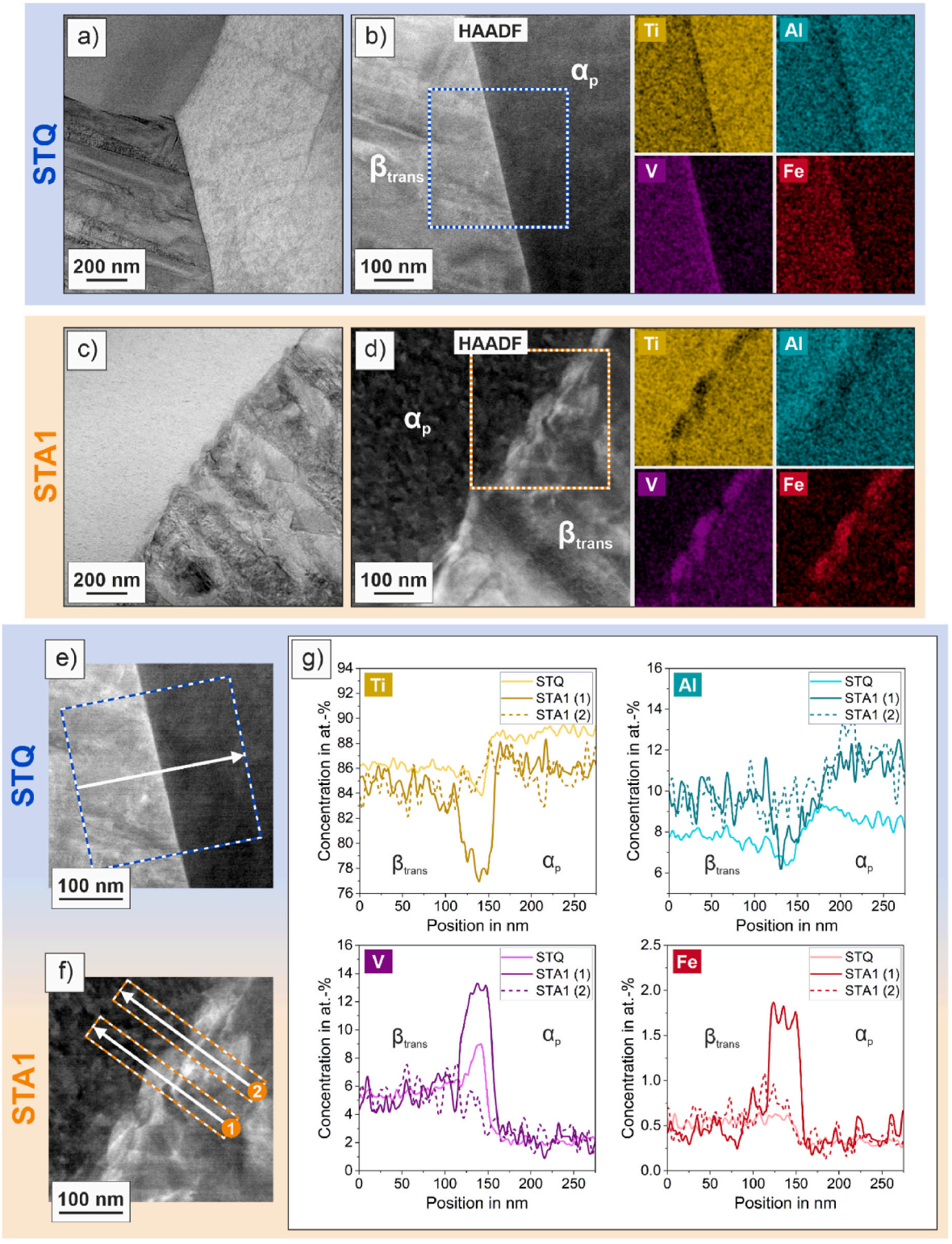

Fig. 3. HRSTEM-(EDS) results of a α_p/β_{trans} interface in STQ- (915 °C, 120 s, WQ) and STA1-state (915 °C, 120 s, WQ + 570 °C, 180 s, AC): a), c) BF overview images; b), d) HAADF close-ups with EDS maps of marked areas. Concentration profiles across the interfaces are shown in g); e) and f) indicate the regions analyzed (HAADF images).

In three-dimensional space, the interfaces that appear as lines in the TEM images correspond to two-dimensional planes. Derived from the 2D-projections, these planes are highly likely to be relatively flat and smoothly curved in the STQ-state. In contrast, they exhibit a significantly higher complexity in the STA-state. It should be noted that the displacive martensitic transformation from the bcc β-phase to the distorted hcp α'-phase is highly likely accompanied by a volume change. This implies that the α_p/β_{trans} interfaces in the STQ-state are not fully relaxed. Against this background, the higher complexity of the α_p/β_{trans} interfaces after short-time annealing may be indicative of partial stress relaxation. This interpretation is further supported by independent evidence for stress relaxation obtained from HEXRD experiments (Section 3.4).

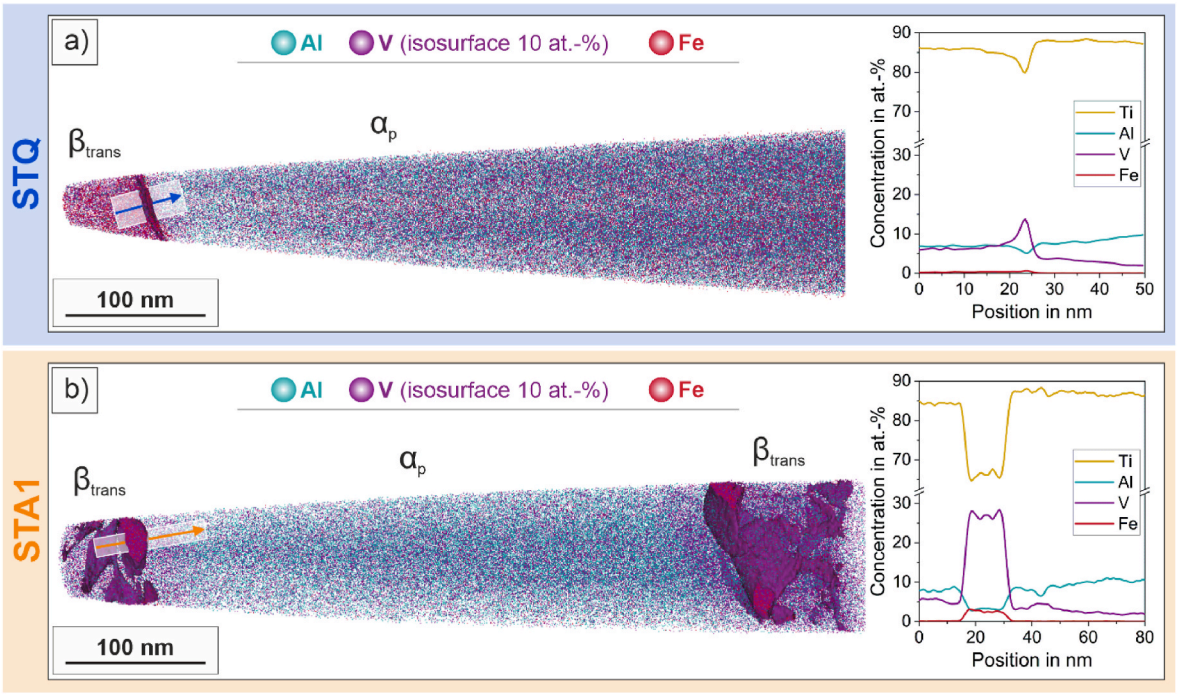

Fig. 4. APT results encompassing α_p/β_{trans} interfaces and corresponding concentration profiles in a) for the STQ (915 °C, 120 s, WQ) and b) the STA1 material state (915 °C, 120 s, WQ + 570 °C, 180 s, AC). The concentration profiles represent proximity histograms, evaluated normal to the interface along the arrow direction. The data were averaged within concentric cylindrical shells, indicated by the semi-transparent, white bordered regions.

In the STQ condition, the α_p/β_{trans} interfaces are decorated with a V-rich interfacial layer (see Fig. 3 b), e), g) and Fig. 4 a)). This layer exhibits a maximum V-content directly at the α_p/β_{trans} interface, exceeding that within the β_{trans} interior. The proxigrams show a gradual decrease in V-concentration from the α_p/β_{trans} interface toward the β_{trans} grain interior. After ~20-30 nm, the V-level approaches that of the β_{trans} interior. The concentration profiles obtained by HRSTEM-EDS and APT are in good qualitative agreement; however, quantitative differences are observed. In HRSTEM-EDS, a non-perfect edge-on interface orientation combined with beam broadening leads to signal contributions from regions above, below, and adjacent to the interface, reducing the apparent segregation magnitude. The higher values measured by APT are therefore considered quantitatively more accurate.

In contrast to the STQ-state, the α_p/β_{trans} interfaces in the STA1-state exhibit clusters enriched in β-stabilizing elements V and Fe. These rounded clusters alternate with interfacial sections depleted in β-stabilizing elements, compare Fig. 3 d), f), g), and Fig. 4 b). For clarification - in this context, the term "cluster" refers to a localized chemical enrichment without explicit information on the underlying crystal structure or phase identity. From both HRSTEM-EDS and APT, it can be deduced that the clusters observed in the STA1-state are more heavily enriched with β-stabilizers than the layer that appears in the STQ-state. Accordingly, the trends from STQ to STA1 are in good agreement when comparing the two methods; however, as in the STQ-state, the maximum element concentrations of the interfacial clusters determined by HEXRD-EDS are lower than in the case of APT. Again, the actual V- and Fe-contents of the V-/Fe-rich clusters are underestimated by HRSTEM-EDS analysis (Fig. 3 g)). In the STA-state, the deviation from the actual composition is even higher than in the STQ-state. This is attributed to the fine, rounded shape of the V-/Fe-rich clusters. As a result, the HRSTEM-EDS analysis inevitably includes regions beneath, above or adjacent to the clusters to a certain extent. From the APT results shown in Fig. 4 b), it is evident that the exemplarily considered V-/Fe-rich cluster at the α_p/β_{trans} interface exhibits a maximum V-content of ~27.5 at.-% and a Fe-content of ~2.5-3.0 at.-%. The adjacent region within the β_{trans} grain (left side of the concentration profile) contains lower levels of β-stabilizers and a higher Al-content compared to the cluster. However, comparing the composition of this inter-cluster region with that of the primary α-phase (right side of the profile) reveals clear differences. Specifically, the contents of β-stabilizing elements are higher, while those of Al and Ti are lower than in the α_p-phase. The findings indicate that V and Fe were expelled from the α'-martensite. Consequently, the inter-cluster regions have chemically evolved towards the α-phase. Nevertheless, their higher Fe- and V-contents compared to the primary α-phase indicate that the redistribution of elements has not yet progressed to a stable state. For completeness, it is noted that a proxigram across a cluster in the lower part of the same STA1 tip (not shown here) yielded similar absolute values and compositional trends as the exemplary case from the upper part presented above.

After analyzing the α_p/β_{trans} interfaces, attention is next turned to sub-structure interfaces within the β_{trans}-grains. To enable a reliable comparison between the STQ- and STA1-state, nano-twin-interfaces within (prior) α'-plates were selected due to their identical misorientation. These interfaces were analyzed in comparable orientations, i.e., oriented edge-on along the same zone axis [12–31]. HRSTEM images of such nano-twins at atomic resolution as well as corresponding HRSTEM-EDS results are shown in Fig. 5. The twins were identified to exhibit a (1-101) twinning plane type relationship, compare Supplementary Note 1, belonging to the {10-11} twinning plane family.

The HRSTEM-EDS element maps of the STQ nano-twin in Fig. 5 b) and the concentration profiles in Fig. 5 g) prove that the interface is slightly enriched in V and Fe and depleted in Ti compared to the surrounding α'-martensite. Furthermore, the concentration profiles indicate that this enrichment extends over only a few atomic layers on either side of the twin interface. This suggests that V-atoms are somehow migrating towards the newly formed interface during the martensitic transformation of prior β-grains.

The HRSTEM-EDS concentration profile of the STA1 nano-twin-interface (Fig. 5 g)) confirms diffusion-driven segregation of the β-stabilizers V and Fe toward the interfaces during short-time annealing. In the STA1-state, the V-/Fe-enriched region around the nano-twin-interface is broader, and the segregation magnitude at the interface is

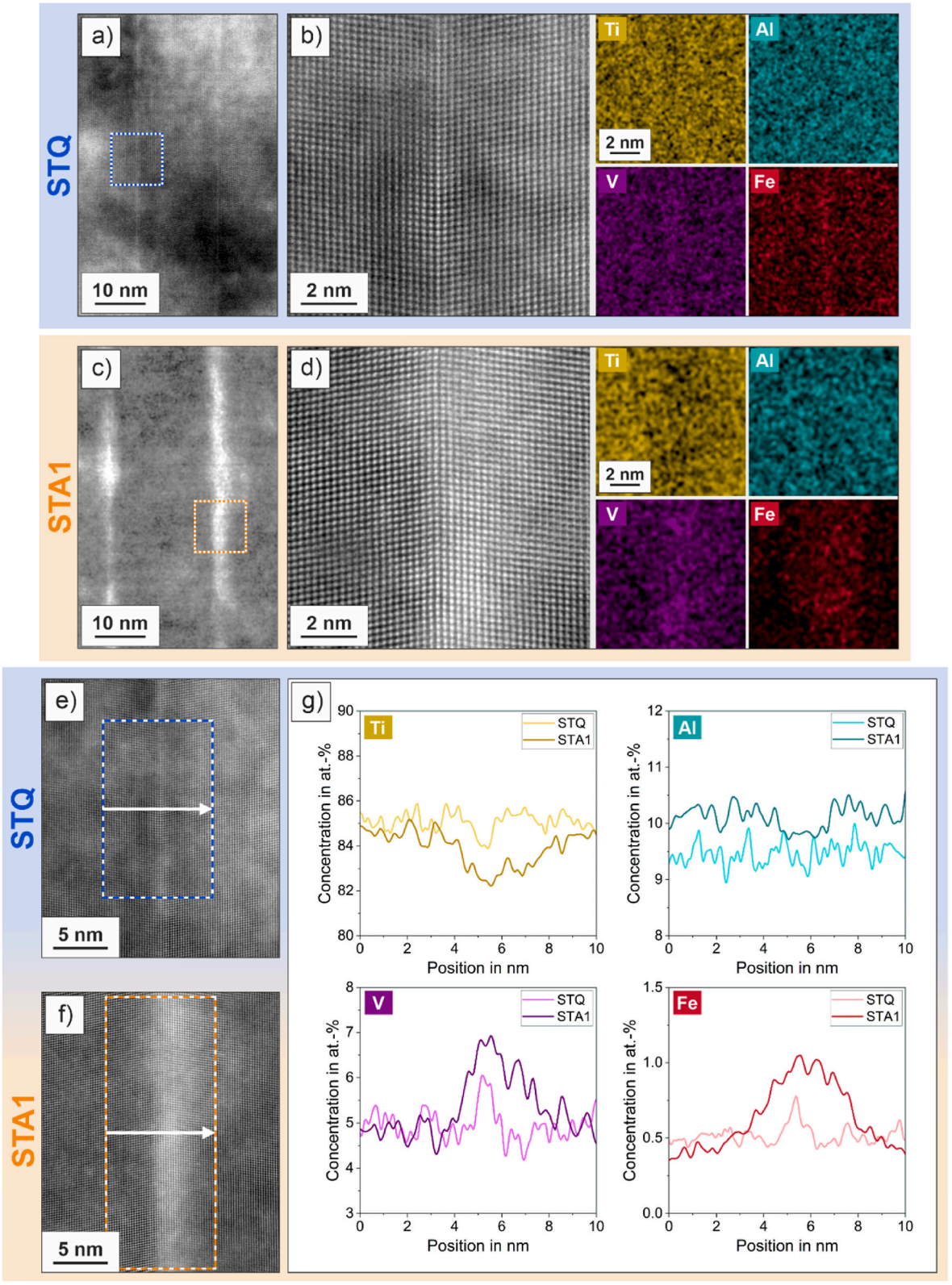

Fig. 5. HRSTEM-(EDS) results of a nano-twin interface within a α'-plate in STQ- (915 °C, 120 s, WQ) and STA1-state (915 °C, 120 s, WQ + 570 °C, 180 s, AC): a), c) overview HAADF images; b), d) higher-magnification HAADF images with corresponding EDS maps. Concentration profiles across the nano-twin interfaces are shown in g);e), f) indicate the areas analyzed (HAADF images).

higher compared to the STQ-state.

APT analysis of a tip extracted from an STA1-β_{trans}-grain, shown in Fig. 6 a), also reveals V- and Fe-enrichments. The observed cluster-like distribution aligns well with the interfacial architecture within β_{trans}, in particular those of α'/α'-interfaces and nano-twins. Fig. 6 b) presents concentration profiles taken from different sites of interest within the STA1-β_{trans}-tip, each across the V-depleted matrix and V-rich clusters. The concentration profiles of sites of interest 2 and 3 demonstrate that

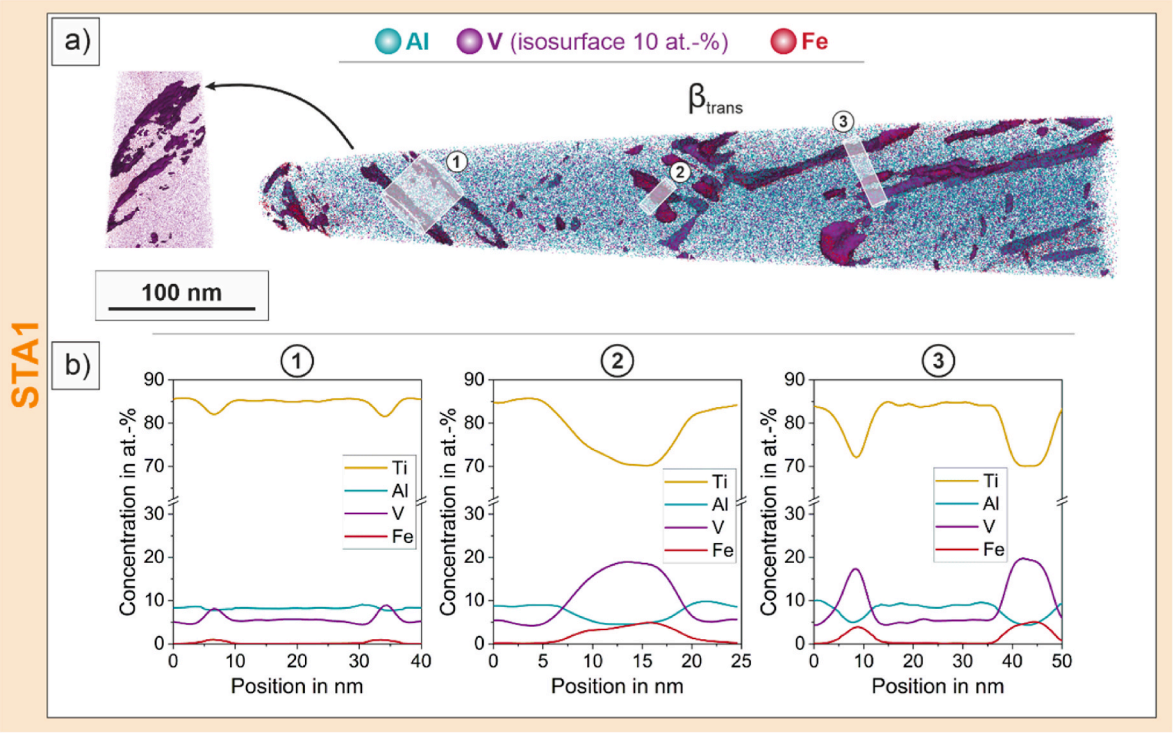

Fig. 6. APT results of the β_{trans} microstructure in STA1 material state (915 °C, 120 s, WQ + 570 °C, 180 s, AC) encompassing nano-twin-interfaces: a) STA1-β_{trans} tip with marked regions of interest and b) corresponding concentration profiles. The concentration profiles represent proximity histograms, evaluated normal to the interface and averaged within concentric cylindrical shells across the clusters, as indicated by the semi-transparent, white-bordered regions.

the regions enriched in β-stabilizers are distinguished by a maximum V-content of ~18-20 at.-% and a maximum Fe-content of ~4.5-5 at.-%. Therefore, the chemical cluster composition within β_{trans} differs from that at the α_p/β_{trans} interface; more precisely, it is characterized by a maximum V-content lower by ~7-10 at.-% and a maximum Fe-content higher by ~1.5-2 at.-%. Further, it can be derived from site of interest 1, see rotated section in Fig. 6 a) and the concentration profile for cylinder 1 in Fig. 6 b), that the distribution of alloying elements at interfaces within β_{trans} is not homogeneous.

Based on the diffusion coefficient values reported by G. Lindwall

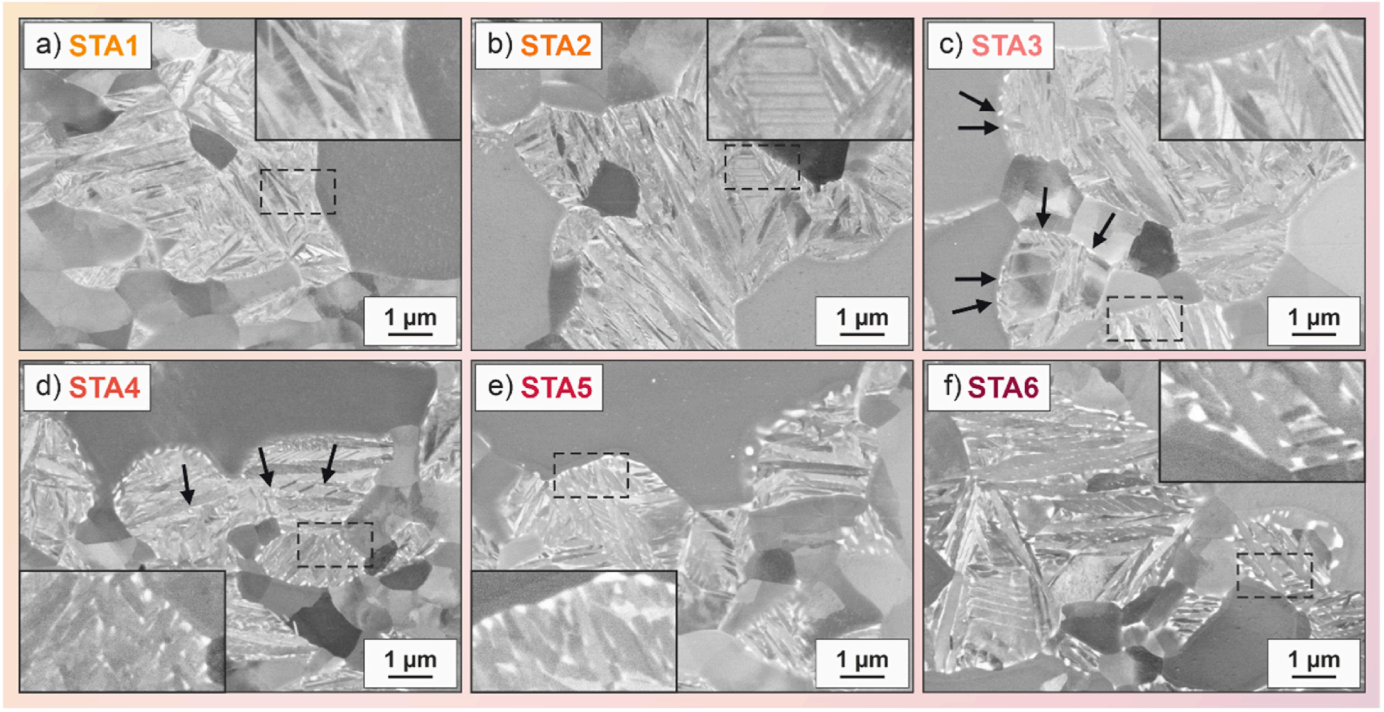

Fig. 7. SEM-BSE microstructural images of different STA-states (915 °C, 120 s, WQ + 570 °C, var. t_A, AC) with t_A for a) STA1: 180 s (3 min), b) STA2: 600 s (10 min), c) STA3: 1800 s (30 min), d) STA4: 3600 s (1 h), e) STA5: 10800 s (3 h) and f) STA6: 21600 s (6 h).

et al. [49], and as described in Supplementary Note 2, the diffusion coefficient of V in hcp α-Ti at 570 °C was extrapolated to approximately 3.5×10^{-19} m^2/s. Using this value, we estimated a diffusion distance of 6.5 nm for the STA1-state. The calculation is based on $t_A = 180$ s and an effective time on target temperature Δt_{eff} of ~60 s (compare Fig. 1 b)). The obtained value should be regarded as an estimate. It is based on a bulk diffusion model and therefore does not account for potential short-circuit diffusion pathways associated with the high density of interfaces, twins, and lattice defects present in α' martensite, nor for grain boundary diffusion or mutual interactions with other alloying elements in α-Ti. In addition, the heating period is neglected. Nevertheless, this estimate is in reasonable agreement with the experimentally observed concentration profiles shown in Fig. 6 b).

3.3. Microstructural evolution during prolonged annealing

The above observed segregation and local enrichment of β-stabilizers at interfaces indicate the onset of an α' → α+β transformation reaction. To further elucidate the microstructural evolution during progressive transformation, SEM-BSE imaging was employed to characterize samples after prolonged annealing times. The resulting microstructures are presented in Fig. 7.

When comparing SEM-BSE micrographs in Fig. 7 a) to f), an increasing occurrence of brighter regions are observed for longer annealing times. Distinctive brighter phases firstly appear after a t_A of 1800 s at the α_p/β_{trans} interface, see arrows in Fig. 7 c). These brighter phases show a round morphology. At higher $t_A \geq 3600$ s, shown in Fig. 7 d)-f), additional bright phases appear at α'/α'-interfaces and nano-twin-interfaces. Since brighter regions in BSE-contrast are typically associated with a higher average atomic number, the appearance of these regions indicates local enrichments of β-stabilizing elements such as V and Fe. The progressive increase of brighter regions with annealing time can be associated with a progressive element partitioning from α' to equilibrium α- (α_{eq}) and equilibrium β-phases (β_{eq}). Due to the occurrence of the brighter regions at α_p/β_{trans}, α'/α' and nano-twin-interfaces, it is considered highly likely that the V-/Fe-enrichments observed after an annealing time of 180 s at these interfaces (compare Section 3.2.2) either already represent β-nuclei with a bcc crystal structure - thereby promoting further accumulation of β-stabilizing elements - or at least serve as precursor sites for β-phase formation. Additionally, it is notable in the SEM-BSE images that the β_{trans}-grains are surrounded by a seam-like structure, which is clearly evident in the SEM-BSE image of the STA6-sample ($t_A = 21600$ s) in Fig. 7 f) and stands out from both the α_p-phase and the β_{trans} microstructure. Closer examination reveals that the seam expands from α_p/β_{trans} grain boundary position x_0 in the direction of the β_{trans}-grains with increasing t_A; for clarification compare Supplementary Note 3. Furthermore, estimated diffusion distances of V in α-Ti for the STA1 to STA6 states, derived using the bulk diffusion approach described above, are provided in Supplementary Note 2.

3.4. Crystallographic phase properties derived from HEXRD

To further rationalize the microstructural evolution, a detailed analysis of the crystallographic evolution from AR to STQ to STA1 to STA6 was conducted using HEXRD.

HEXRD spectra of AR, STQ and STA1 states have already been compared in a previous publication by N. Pfeffer et al. [25]. It is worth noting that in the case of material states consisting of both α- and α'-phases (e.g., the STQ-state in this work), the peaks of both phases substantially overlap in HEXRD 1D-spectra due to their similar lattice parameters and lattice geometry. Consequently, it is not possible to distinctly differentiate between these two phases through mere visual inspection. However, in [25] it was shown that the HEXRD spectrum of the STQ material is characterized by the appearance of broader α/α'-peaks and the absence of β-peaks in comparison to the as-received state, in which only pure α- and β-peaks are known to occur. This peak broadening, as well as the flatter narrowing of the α/α'-peaks and the partially asymmetrical appearance is attributable to the presence of the martensitic α'-phase.

Fig. 8 a) – c) compares HEXRD spectra of the STQ-state and the STA-states. It is evident that the α/α' peak width undergoes a slight decrease from STQ to STA1, i.e., after a short annealing time of only 180 s at 570 °C, compare Fig. 8 b). This observation indicates a reduction in internal stresses and a relaxation of the martensitic unit cell towards those of the hcp α-phase, even after this short annealing time. The occurrence of small β-reflections in the STA1 condition (see, for instance, Fig. 8 c)) indicates a phase transformation of small regions to the bcc β-phase. These regions most likely correspond to those with an increased V-/Fe-content within β_{trans}, as identified in Section 3.2.2.

As the annealing time increases from STA1 to STA5, the height of the β-peaks increases markedly, reflecting an increasing β-phase fraction with increasing annealing time. This provides evidence for progressive transformation along the α' → α+β pathway, consistent with the trend indicated by SEM-BSE in Section 3.3. Additionally, the peak width of the α/α'-peaks changes with t_A, sometimes asymmetrically. For instance, when examining the α/α' (002) peak, a peak narrowing becomes evident, starting from larger diffraction angles, and a shift of the (002) peak maximum to smaller diffraction angles, i.e., to larger lattice parameters according to the Bragg's law.

Rietveld refinement enabled a quantification of the phase fractions of α, β and α' as well as their lattice parameters for the considered states (AR, STQ, STA1-6). As mentioned in the experimental section, the α- and α'-phase in the STQ-state were fitted separately. Calculated spectra for sum, α, and α' relative to the observed one are demonstrated by the excerpt in Fig. 8 d). In contrast, a single hcp phase was fitted for the STA-states. Additionally, the microstrain of the hcp and bcc phases was determined using the full width at half maximum (FWHM) of the peaks, following the Williamson-Hall method [50]. It should be noted that any potential influence of grain size on the microstrain from STQ to STA6, which is assumed to be minimal, was neglected in this analysis.

First, Fig. 9 a)-d) provide information on the fractions of hcp phases and their lattice parameters a and c and lattice geometries (via c/a ratio) and e)-f) on phase fraction and lattice parameter of the bcc β-phase (a_β).

A comparison of the phase fractions in Fig. 9 a) and e) reveals the following trends: In the AR-state, Rietveld refinement yields phase fractions of 96.1 % α and 3.9 % β. After STQ treatment, the microstructure consists of ~48.6 % α' besides 51.4 % α with no detectable β-phase. These results are in good agreement with the fractions obtained via phase binarization in [25]. Within the STA-states, the β-phase fraction increases steadily from ~1.1 % ($t_A = 180$ s) to ~4.2 % ($t_A = 21600$ s) with t_A and approaches an equilibrium state after 10800 s consistent with the fraction in the AR-state.

Examining the lattice parameters of the α- and β-phases in the AR-state, Fig. 9 b), c) and f), reveals the following: the α-phase lattice parameters, with $a_\alpha \approx 2.923$ Å und $c_\alpha \approx 4.668$ Å, deviate from those reported for high-purity Ti ($a \approx 2.950$ Å, $c \approx 4.683$ Å, and $c/a \approx 1.587$ [51]). However, they are in good agreement with values reported for the α-phase in slowly cooled Ti-6Al-4V ($a_\alpha = 2.925 \pm 0.002$ Å, $c_\alpha = 4.670 \pm 0.005$ Å, $c/a \approx 1.597$ [52]). The β lattice parameter, with $a_\beta = 3.184$ Å, differs from the extrapolated value for bcc high-purity Ti at room temperature ($a = 3.283$ [53]). The deviations of the lattice parameter values obtained in this work from those reported for high-purity Ti are primarily attributed to the influence of alloying elements on the lattice parameters, although processing may also have exerted a minor effect.

Fig. 9 b) and c) confirm that the hexagonal cell of the α'-martensite in STQ-state is characterized by a larger a lattice parameter and a smaller c lattice parameter compared to the α_p- or α-phase in the STQ- and the AR-state. This is associated with a smaller c/a ratio of the hexagonal α' cell (see Fig. 9 d)). This finding is consistent with observations reported in literature, which compare the hexagonal cell of α' in the fully-martensitic microstructure case with that of the (near-)equilibrium α-phase in α+β microstructures [54,55]. Therefore, the observed

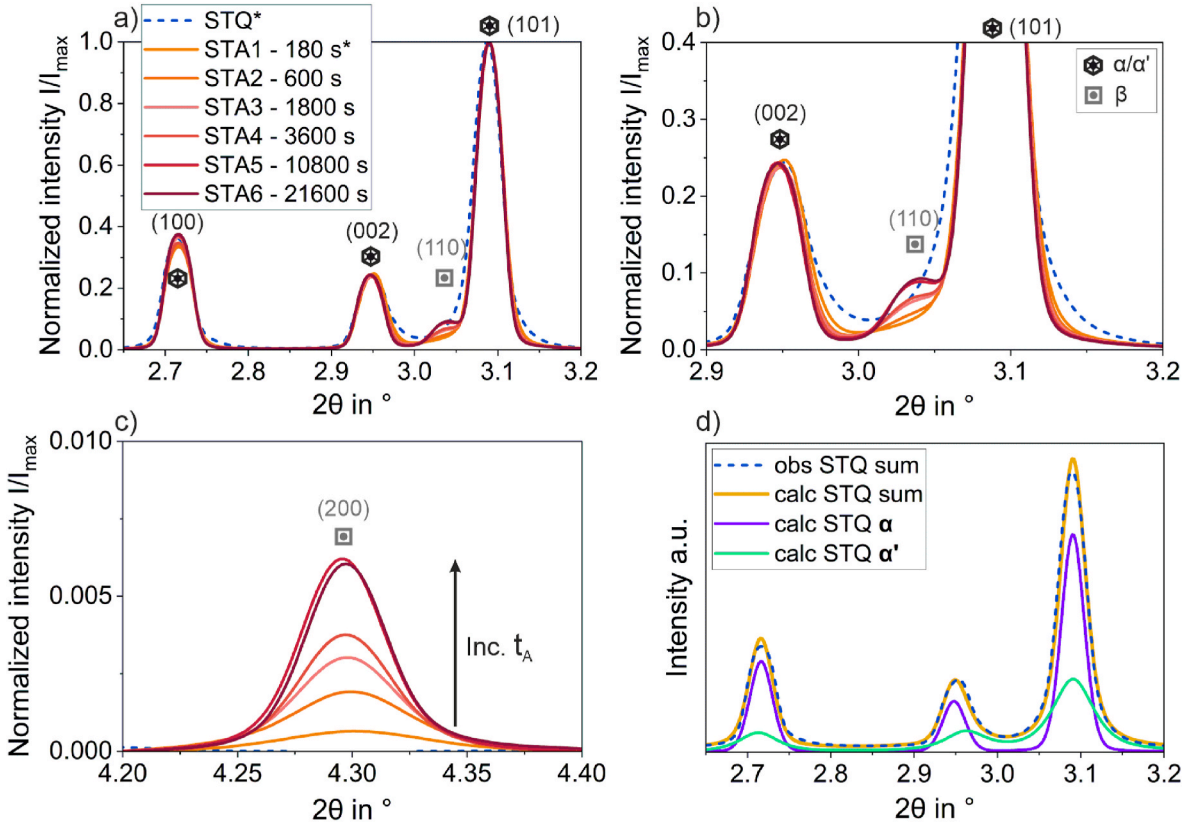

Fig. 8. a) – c) Selected excerpts from HEXRD spectra of different material states: STQ state (915 °C, 120 s, WQ) and various STA states (915 °C, 120 s, WQ + 570 °C, varying t_A, AC) and d) observed HEXRD spectrum of the STQ state and corresponding calculated spectra via Rietveld refinement. An asterisk (*) indicates data that have been reported previously in [25].

differences between the α and α' hcp lattice properties are mainly attributed to the displacive character of the transformation β (bcc) → α', which imposes a distorted hcp lattice with a non-ideal, energetically unfavorable *c/a* ratio. Moreover, the chemical compositions of the phases likely also contribute, at least to some extent, to both the absolute values and the relative differences of the lattice parameters between α and α' [14,51,56–59].

A comparison of the *c/a* ratios for the STQ and STA1 states in Fig. 9 d) clearly shows that the martensitic lattice geometry rapidly approaches an energetically preferred configuration close to that of the α_p-phase even after a short annealing time (STA1, $t_A = 180$ s). Accordingly, from a crystallographic point of view, the former α'-phase can no longer be classified as such after $t_A \geq 180$ s, but is more accurately described as α-phase supersaturated with β-stabilizing elements. Since the observed crystallographic α'-decomposition occurs simultaneously to the chemical redistribution (as shown above), the term "martensite decomposition" will hereafter refer to the combination of both processes. As the annealing time t_A increases from STA1 to STA6, there are additional, though moderate, changes in the *c/a* ratio and the lattice parameters *a* and *c* (Fig. 9 b) and c)). These alterations are attributed to the progressive relaxation and the increasing formation of β-phase, with the latter being associated with a further partitioning of the alloying elements between α and β.

The lattice parameter of the β-phase initially increases substantially from STA1 ($t_A = 180$ s) to STA3 ($t_A = 1800$ s), see Fig. 9 f). After that, the time-related rate of change decreases towards STA5 ($t_A = 10800$ s). Studies on the Ti-V binary system [60,61] demonstrated that a reduction in V-content increases the β lattice parameter. It is conceivable that the β-nuclei with a bcc structure detected after 180 s originate primarily from clusters at the α_p/β_{trans} interfaces, as these regions are more enriched in β-stabilizers, or more precisely, show a different chemical composition than those in the β_{trans} interior. With longer annealing times, these nuclei are expected to grow, and additional nuclei form from V-/Fe-enriched regions inside the β_{trans} grains. However, the newly formed nuclei are likely to contain lower levels of β-stabilizers and higher Al-content compared to the previously formed nuclei. This could account for the observed increase in the overall β lattice parameter. Once the β phase fraction is close to the equilibrium, the element concentrations in different β-regions are expected to gradually equalize. The only minor difference in the determined β lattice parameter between STA5 and STA6 suggests that equilibrium has been reached.

For the quantitative evaluation of peak broadening, the diffraction reflections were analyzed using the Williamson–Hall approach. For this purpose, the integral peak breadth cos(θ) • 10^3 was plotted against 4 sin(θ) (Williamson–Hall plot). The slope of the resulting linear fit yields the isotropic microstrain of the respective phase. Fig. 10 shows the Williamson-Hall plots as well as the corresponding values of the isotropic microstrain for the investigated material conditions.

Regarding the microstrain in the hcp phases, the following conclusions can be drawn from Fig. 10 a) and b): The martensite in the STQ-state exhibits a significantly higher microstrain than the α-phase in the AR- and STQ-state and the hcp phase in the STA-states. This was already evident from the peak widths in Fig. 8. From STA1-to STA6-state, the microstrain of α-phase was found to decrease continuously with increasing annealing time. The AR-state shows the lowest microstrain among all investigated stress state of the present study. However, after annealing at 570 °C for 21600 s, followed by air cooling, a similarly relaxed state of the α-phase was attained.

Fig. 10 c) and d) show that the microstrain of the β-phase as a function of t_A exhibits a similar trend to that of the α-phase. In particular, the microstrain of the β-phase decreases from STA1 to STA6, approaching the microstrain of the β-phase in the AR-state. Possible

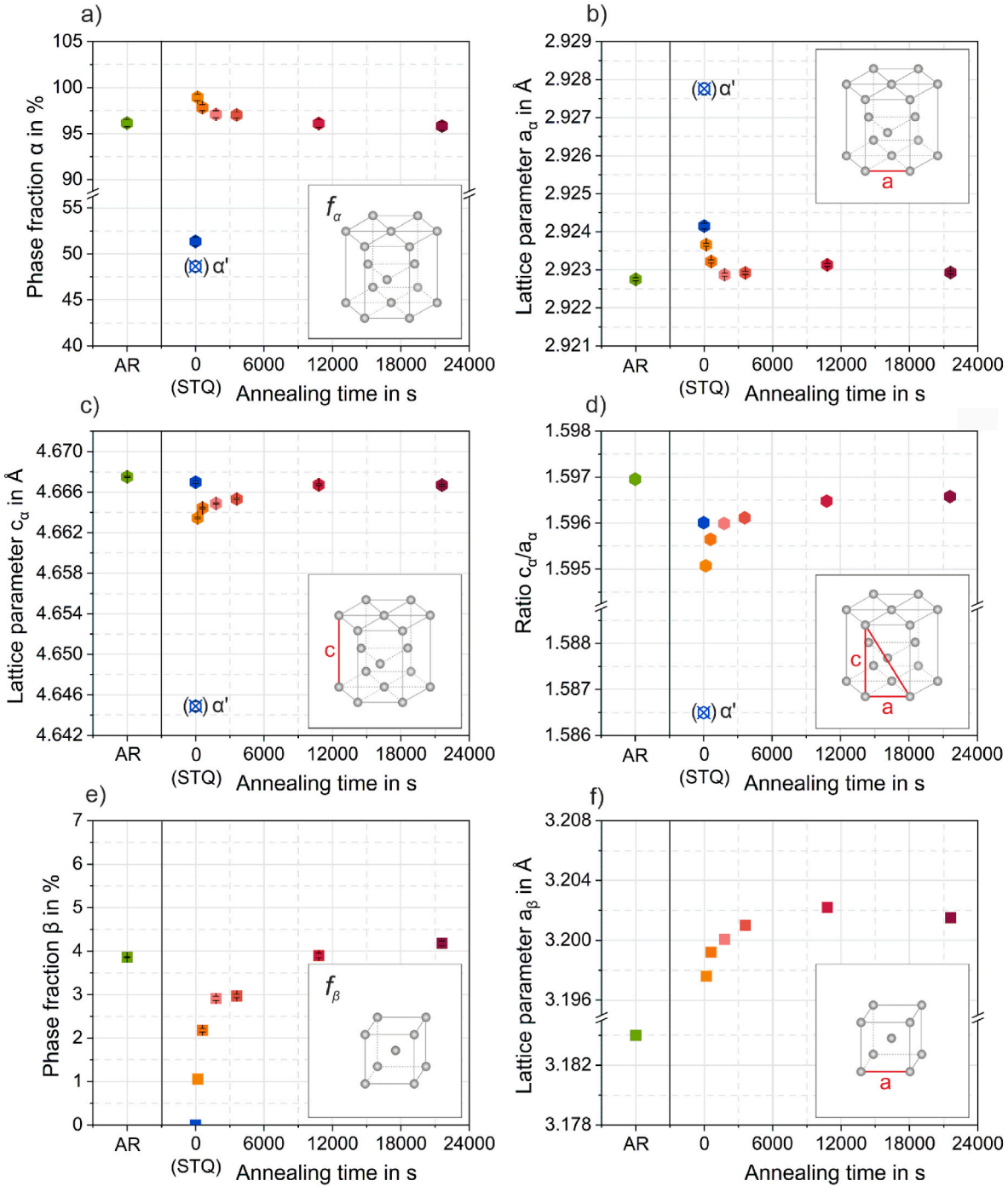

Fig. 9. Crystallographic phase properties for different Ti-6Al-4V material states determined by Rietveld refinement: a) phase fraction of the α-phase, b) and c) lattice parameters *a* and *c* of the α-phase and d) *c/a* ratio reflecting the lattice geometry of the hcp unit cell, e) phase fraction of the β-phase and f) lattice parameter of the β-phase. For the STQ-state, data for α' are additionally included (unfilled crossed blue data points) and labeled accordingly.

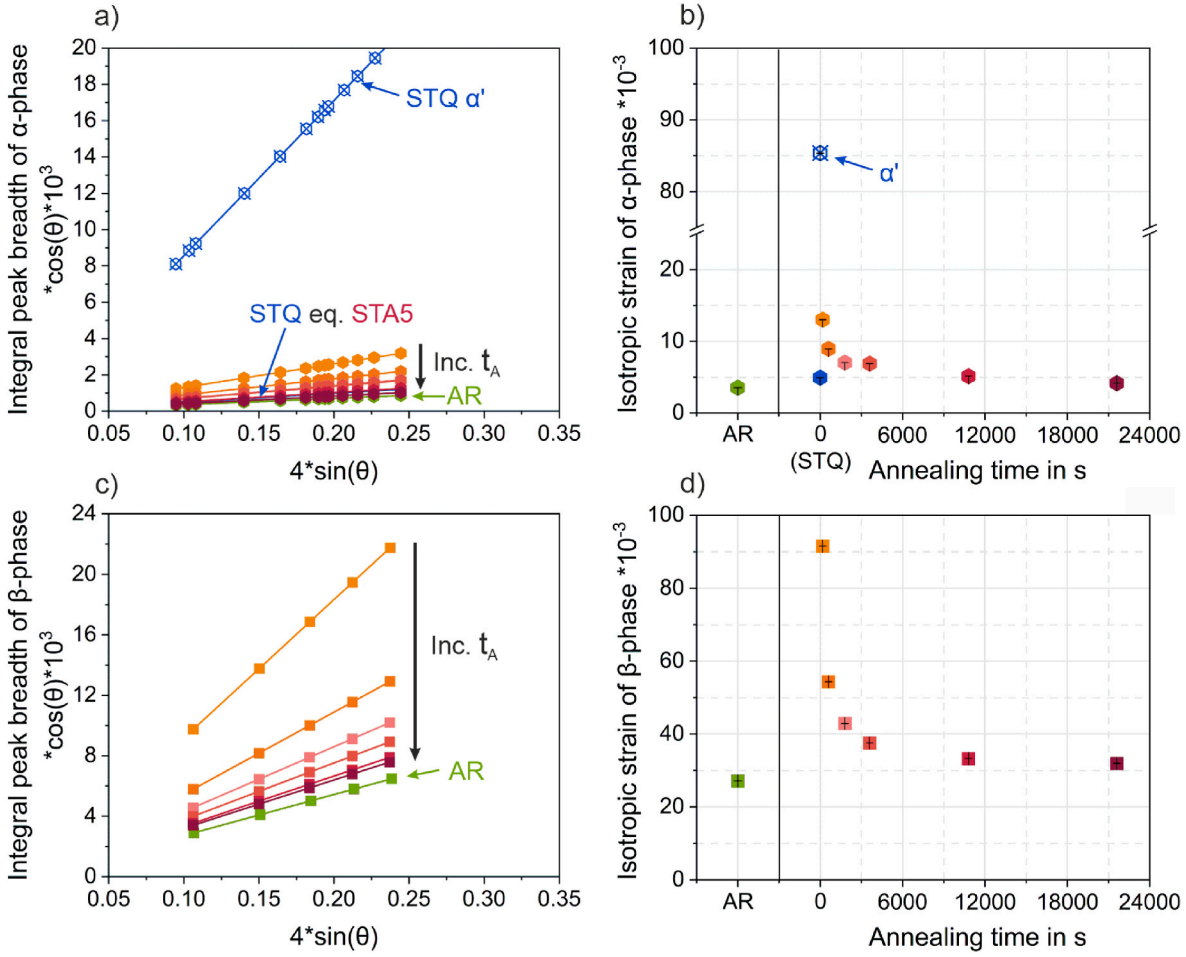

Fig. 10. Microstrain analysis of phases in different Ti-6Al-4V material states, based on refined spectra: a) Williamson-Hall plots for the hcp α-phase, b) corresponding isotropic microstrain values for the α-phase, c) Williamson-Hall plots for material states containing the bcc β-phase, and d) corresponding isotropic microstrain values for the β-phase. For the STQ-state, data for α' are additionally included (unfilled crossed blue data points) and labeled accordingly.

origins of the observed parallel trend between the hcp and bcc phases will be addressed/discussed in Section 4.1.

3.5. Tensile behavior

Fig. 11 provides representative stress-strain curves for the AR-state, the STQ-state and three STA-states and Table 2 corresponding mean values for the yield strength at 0.2 % plastic deformation (YS), the ultimate tensile strength (UTS), the delta between UTS and YS (UTS-YS), the uniform elongation (UEL) and the elongation at fracture (ELF).

The strength data for the AR, STQ, and STA1 conditions have been previously reported and discussed in [25]. Of particular relevance to the present study is the finding that the strength of the STQ condition can be significantly enhanced by a subsequent (short-time) annealing. The present results further reveal that annealing at 570 °C leads to systematic changes in the tensile response as the annealing time increases from STA1 to STA6: strength decreases, while the UEL increases markedly. Additionally, a gradual trend towards a more pronounced YS with increasing t_A is observed. Furthermore, the work-hardening rate (WHR) decreases from STA1 to STA4, while similar values are observed for the AR, STA4, and STA6 material states.

Table 2
Mean yield strength at 0.2 % plastic strain (YS), mean ultimate tensile strength (UTS), ΔUTS-YS, mean uniform elongation (UEL), and mean total elongation at fracture (ELF) for different material states: AR (as-received), STQ (915 °C, 120 s, WQ) and STA material states (STQ + 570 °C, var. t_A, AC) with $t_A = 180$ s for STA1, $t_A = 3600$ s for STA4 and $t_A = 21600$ s for STA6. The values were built from a minimum of three valuable tests (N ≥ 3). An asterisk (*) indicates data that have been reported previously in [25] for N ≥ 3.

Material state	YS in MPa	UTS in MPa	UTS-YS in MPa	UEL in %	ELF in %
AR*	987 ± 3.0	1080 ± 3.9	93 ± 3.6	6.7 ± 0.46	15.4 ± 0.39
STQ*	839 ± 9.8	1076 ± 5.0	237 ± 10.6	10.2 ± 0.30	18.8 ± 0.95
STA1	1111 ± 1.6	1226 ± 3.3	114 ± 3.3	3.6 ± 0.14	12.0 ± 0.85
STA4	1086 ± 7.3	1181 ± 5.3	95 ± 3.3	4.4 ± 0.21	12.3 ± 0.25
STA6	1062 ± 6.8	1152 ± 3.9	90 ± 6.4	5.1 ± 0.28	12.9 ± 0.13

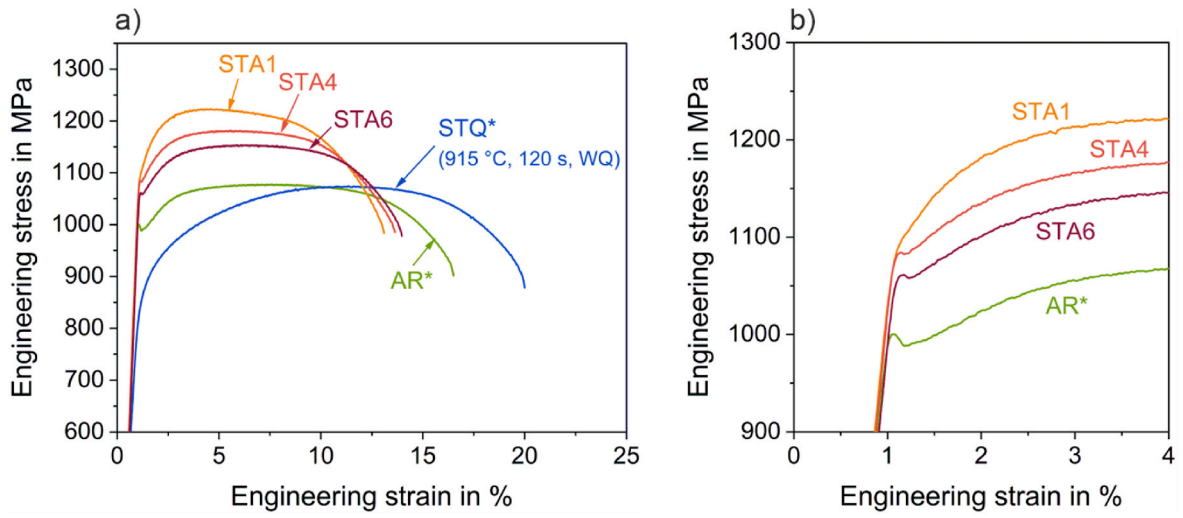

Fig. 11. Representative stress-strain curves for different material states: AR (as-received), STQ (915 °C, 120 s, WQ) and STA material states (STQ + 570 °C, var. t_A, AC) with t_A = 180 s for STA1, t_A = 3600 s for STA4 and t_A = 21600 s for STA6. An asterisk (*) indicates data that have been reported previously in [25].

4. Discussion

4.1. Microstructural evolution of α+α' Ti-6Al-4V during annealing

By combining the results of this study with findings from literature, the microstructural evolution of α+α' Ti-6Al-4V (solution heat treatment: 915 °C, 120 s, WQ) during subsequent annealing (+570 °C, ≤21600 s, AC) can be described as follows. The schematic in Fig. 12 illustrates the chemical redistribution of the alloying elements along the applied heat-treatment path.

4.1.1. STQ-state

In the STQ α+α' microstructure, the present α'-martensite results from a displacive transformation from bcc β to hcp α', exhibiting several characteristics due to its non-diffusional transformation that is based on shear deformation.

Morphological appearance and internal structure: The martensite forms as numerous α'-plates, introducing a high density of α'/α' interfaces and nano-twins within α' upon quenching (compare Fig. 2 g)-h), and scheme Fig. 12 a)). In the literature, coherent transformation twins with a twinning plane of the {10-11} type within the α'-plates have been frequently reported for titanium-based alloy systems [16,37,41,62,63], which is the same type as identified for the twins in Fig. 5. However, twins of the {10-12} and {11-22} plane types have been also observed in some cases [5,64].

Chemical supersaturation: The α'-martensite retains the chemical composition of the β-phase, resulting in supersaturation with β-stabilizing elements. This is evidenced by HRSTEM-EDS analyses (Fig. 3 b) and EDS-results from previous work by N. Pfeffer et al. [25] and represented by scheme Fig. 12 a).

Elemental segregation at interfaces: Slight enrichment in β-stabilizers V and Fe is detected at α'/α' and nano-twin interfaces, with corresponding depletion in adjacent atomic layers (see Fig. 5 b), g) and scheme Fig. 12 a)). This suggests that V and Fe atoms locally segregate to newly formed interfaces either during martensitic transformation or upon further cooling below the martensite finish temperature M_f. Recent work by D. Wen et al. [65] indicates that short-range segregation over a few atomic layers is possible during a very short time interval. Further, an incremental estimate of the diffusion distance of V during water quenching between a potential M_f and room temperature, based on the data provided by G. Lindwall et al. [49] (see Supplementary Note 4), suggests that diffusion distances in the order of only a few atomic layers are possible. However, it must be considered that the M_f value of 710 °C after [17] used in this estimation may differ from the actual transformation temperature, as it is likely sensitive to the chemical composition of the β-phase before quenching. Moreover, the obtained diffusion distances should again be regarded as estimates. The diffusion coefficient employed represents bulk diffusion behavior in α-Ti and does not account for potential short-circuit diffusion pathways associated with interfaces, lattice defects, and stress fields that dynamically form during quenching and martensitic transformation, nor for mutual interactions with other alloying elements. More pronounced V-enrichment at α_p/β_{trans} interfaces may originate from segregation during solution heat treatment and subsequent retention during quenching, from increased driving forces at incoherent interfaces or from short-range atomic displacements associated with the formation of martensite plates, which may shift near-interface V atoms toward the α_p/β_{trans} interface.

Lattice distortion and internal stresses: the martensitic α'-phase is characterized by a high level of elastic lattice distortion and high degree of stored energy, which is reflected by HEXRD results in Figs. 8 d) and Fig. 10 a) and b). The lattice parameters of the α'-phase differ from those of the α-phase (Fig. 9 b)-d)), which is mainly attributed to the lattice correspondence between the prior β-phase (i.e. the β-phase present at the solution heat treatment temperature) and the α'-martensite. Furthermore, internal stresses are expected to accumulate along the α_p/β_{trans} interfaces due to the volumetric change associated with the β → α' transformation.

In summary, the martensite remains in a metastable state at room temperature, characterized by high energy due to both its chemical composition and the structural distortions of the hcp lattice, with a kinetically limited driving force to transition into a more stable state.

4.1.2. Martensite decomposition and segregation of β-stabilizers to interfaces (T_A = 570 °C, t_A = 180 s)

The provision of thermal energy throughout the annealing process initiates a number of ongoing concurrent and interlinked microstructural processes. These processes work to minimize the free energy G of the whole Ti-6Al-4V system with ΔG acting as driving force and to restore thermodynamic equilibrium ($\alpha_{eq}+\beta_{eq}$). According to the Ti-6Al-4V phase equilibrium at annealing temperature, α'-martensite tends to decompose predominantly into α-phase, accompanied by a smaller fraction of β-phase. This transformation process, however, requires chemical redistribution within β_{trans}.

As shown in this study, one underlying process is the diffusion-based migration of the α_p/β_{trans} interface towards the higher-energetic α'-grain (Fig. 7, schemes Fig. 12 c)-e)). This results in the accumulation of the

supersaturated solute elements, specifically V and Fe, at the migrating α_p/β_{trans} interface front. These elements cluster into ellipsoidal V-/Fe-rich allotriomorphs at the α_p/β_{trans} interface, causing local solute depletion in adjacent regions, see Fig. 3 d), f), g) and scheme in Fig. 12 c). The rounded shape arises from an energetically favorable surface-to-volume ratio. Its rapid formation is attributed to enhanced elemental diffusion along grain boundaries, particularly pronounced in the case of high-angle boundaries. Notably, there is a similarity to the initial stages of microstructural formation described for cellular precipitation [66]. As a result of this α_p/β_{trans} boundary migration and the formation of V-/Fe-rich clusters, there is a corresponding decrease in solute atoms in the areas through which the boundaries have traveled (Fig. 3 f) and g), Fig. 4 b)). The wave-like appearance of the STA1 α_p/β_{trans} interface is likely related to the stress-relaxation of the α_p/β_{trans} interface and/or a pinning effect of the V-/Fe-rich clusters.

Beyond the α_p/β_{trans} interfaces, V-/Fe-rich clustering was also observed within the β_{trans}-grains, where α'/α' and nano-twin-interfaces act as segregation sites for V and Fe (compare Fig. 5 d) and g), Figs. 6 and 12 c)). The inhomogeneous enrichment of β-stabilizers at these interfaces (Fig. 6) is attributed to preferential segregation at specific interfacial sites, e.g. such under comparatively high compressive stresses [63]. Further, the appearance of different interface characters, namely α'/α' and internal twins, may affect segregation tendencies due to differing attraction forces for β-stabilizers. Variations in phase fractions and lattice parameters with increasing annealing time (Fig. 9) as well as chemical phase properties of STA1-state (Fig. 6) reveal that $t_A = 180$ s is insufficient to achieve a full chemical redistribution, respectively a $\alpha+(\alpha_{eq}+\beta_{eq})$ microstructure.

From a crystallographic perspective, a significant reduction in elastic distortion of the hcp α'-lattice was observed after only 180 s of annealing

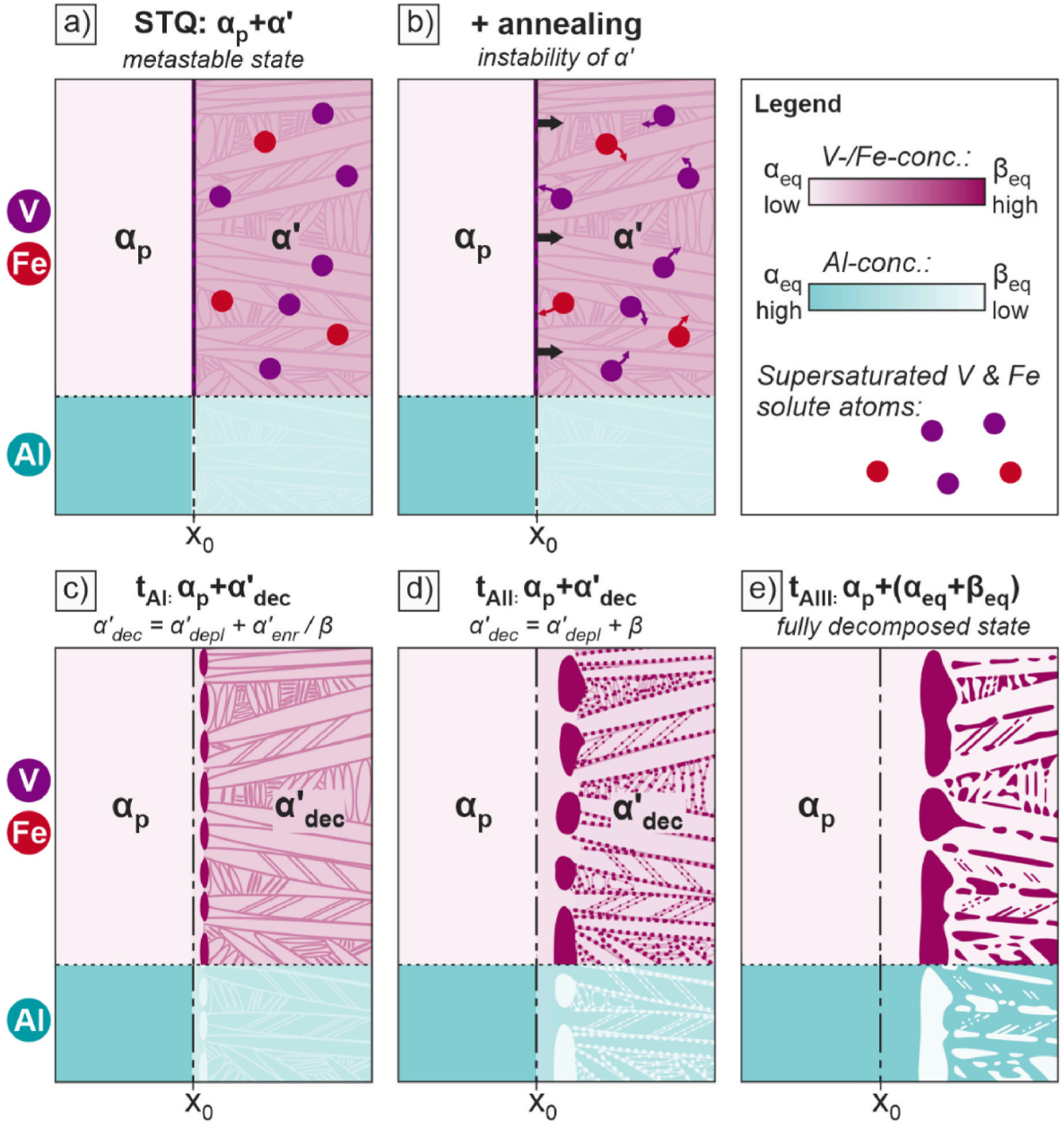

Fig. 12. Schematic representation of the chemical redistribution at the α_p/β_{trans} interface and within β_{trans} during annealing: a) microstructural situation in the STQ state with the 0-position of the α_p/β_{trans} interface (x_0) marked, b) representation of the microstructural tendency driven by the application of thermal energy during annealing. c) and d) represent intermediate states of the progressive martensite decomposition $\alpha' \rightarrow \alpha_{eq}+\beta_{eq}$, with former α'-phase depleted in β-stabilizers referred to as "α'_{depl}" and enriched in β-stabilizers as "α'_{enr}" and e) equilibrium state, with a α_{eq} and β_{eq} structure.

at 570 °C, compare Fig. 10 a) and b). This is mainly attributed to the fact that the martensitic α'-phase, due to the lattice correspondence with the prior β-phase, is constrained into an elastically not fully relaxed configuration. During annealing, thermally activated atomic movements are assumed to enable the lattice to rapidly relax from this state into a more favorable, less distorted configuration. However, to some extent, dislocation annihilation (as observed and described by S.A. Oh et al. [55] for the initial stage of the martensite decomposition in LPBF Ti-6Al-4V) and the chemical redistribution of alloying elements could also be involved in this crystallographic transition.

In summary, the initial annealing stage is marked by a pronounced reduction in microstrain and a strong evolution of the α' lattice parameters towards those of the α-phase, whereas the β phase fraction increases only moderately. The correlated evolution of these parameters suggests that α' lattice relaxation dominates at $t_A = 180$ s, while only initial stages of the α' → α+β transformation are initiated.

4.1.3. Progressive redistribution of alloying elements ($T_A = 570$ °C, $t_A > 180$ s)

With increasing annealing time, the redistribution of alloying elements within β_{trans} progresses gradually until saturation is reached and a relaxed $\alpha_{eq}+\beta_{eq}$ equilibrium microstructure is established. The process is reflected by changes in phase fractions, lattice parameters and microstrains of both phases (Figs. 9 and 10).

With increasing annealing time, the β phase fraction increases gradually. During this process, V-/Fe-rich clusters or bcc β-nuclei located at α_p/β_{trans} interfaces and at interfaces within β_{trans} act as preferred sites for further β-phase formation (compare STA1 HRSTEM-EDS and APT results from Section 3.2.2 with Fig. 7).

The continuous but moderate increase in β phase fraction and the changes in lattice parameters occur in parallel with a similarly moderate and continuous decrease in α lattice strain with increasing annealing time. This simultaneous response provides clear evidence for progressive chemical redistribution within β_{trans} and ongoing α' → α+β transformation. In contrast, a purely recovery-driven or stress-relaxation process would primarily reduce lattice strain without causing systematic changes in phase fractions and lattice parameters. However, a concurrent reduction in dislocation density cannot be excluded as an additional contributor to the release of stored distortion energy in the α lattice.

The correlated evolution of α- and β-phase lattice strain as a function of annealing time suggests crystallographic interplay between the individual phases. In the STA1 condition, incomplete relaxation of the former α'-lattice may introduce adaptation strain in the adjacent β-phase, for example to maintain a defined orientation relationship such as that according to Burgers [18]. Additionally, compositional variations between the β-phase at α_p/β_{trans} and α'/α' interfaces (cf. Fig. 4 b) and Fig. 6) as well as between α_p and the decomposition-derived α-phase, may affect the determined lattice strain state of the hcp and bcc phases.

At longer annealing times, the system reaches a compositionally and structurally stabilized state, consistent with phase equilibrium (scheme Fig. 12 e)). This interpretation is supported by HEXRD results (Figs. 9 and 10), which show no further significant changes in phase fractions, lattice parameters and lattice strain beyond 10800 s of annealing. Since the formation of the β-phase involves not only the enrichment of β-stabilizing elements but also a corresponding depletion of Al in specific regions, it can be assumed that the diffusion rates of alloying elements play a decisive role in determining the time required to reach this stabilized state.

In the stabilized STA6 state, the β-phase appears slightly coarser at former α_p/β_{trans} interfaces than at former α'/α' and nano-twin-interfaces, attributed to the initially higher V availability at α_p/β_{trans} interfaces in the STQ-state in combination with the likely higher driving force for segregation towards and along high angle grain boundaries.

4.2. Comparison with the α' → α+β transformation reaction in LPBF- and fully-martensitic microstructures

The V-/Fe-rich clusters observed in the STA1-β_{trans}-grains resemble the findings reported in the literature on Ti-6Al-4V processed via LPBF in the as-built state, as documented by J. Haubrich et al. [33], M.V. Pantawane et al. [32], and H. Wang et al. [34]. During a single LPBF cycle, the material is heated above T_β, and rapid cooling produces a fully martensitic structure in the deposited layer. In the subsequent layer-by-layer buildup, transient thermal peaks repeatedly affect the underlying layers until they remain unaffected after a certain number of depositions. The cumulative effect of these thermal cycles has been shown to promote the formation of V-/Fe-rich clusters as precursors of the β-phase in the as-built material, indicating the onset of martensite decomposition towards thermodynamic equilibrium (α' → $\alpha_{eq}+\beta_{eq}$). J. Haubrich et al. [33] reported V-/Fe-enrichments at α'/α'-interfaces, while M.V. Pantawane et al. [32] additionally detected V-rich clusters within the martensite plates. H. Wang et al. [34] observed the accumulation of β-stabilizers at α'/α'-interfaces and characterized these regions still as hexagonal α-phase but with elevated Mo_{eq}-content. In [33], the element partitioning ratio $k^{-1} = C_\beta/C_\alpha$ into the β-phase was determined to be one order of magnitude higher for Fe than for V. Similar tendency is derivable from our results presented in Fig. 6.

Relevant literature on other alloy systems further supports the findings of this study. C. Liu et al. [63] investigated the binary Ti-4Mo system with a fully-martensitic initial structure, annealed at 400 °C for 4 h and 500 °C for 8 h. The resulting β precipitates exhibited a Potter orientation relationship with both the α'-phase and the twin boundary, $(01\text{-}1)_\beta \,||\, (10\text{-}11)_{\alpha'}$ and $[-111]_\beta \,||\, [-1210]_{\alpha'}$. In contrast, heterogeneous β-precipitation at α'/α' interfaces and within martensite plates followed the conventional Burgers orientation relationship. Complementary first-principles calculations indicated that Mo segregation to compression sites at coherent twin boundaries is energetically favorable. Calculated segregation energies for alternative β-stabilizers revealed that besides Mo, the elements Nb, Cr, V, and Fe, also exhibit a tendency to segregate to these compression sites [63].

At this point it is worth emphasizing that the chemical composition of the martensite in dual-phase α+α' Ti-6Al-4V is different from that of the martensitic structure in fully-α'-martensitic Ti-6Al-4V, as for example found in the as-LPBFed or the from above T_β as-quenched state. In the fully-martensitic case, the average martensite composition corresponds to the nominal alloy composition [19]. In contrast, α'-martensite in dual-phase α+α' microstructures exhibits higher concentration of β-stabilizing elements V and Fe, but less of α-stabilizer Al. This results from element partitioning between the α- and β-phases during sub-T_β solution heat treatment prior to quenching, with the β composition depending on the solution heat treatment temperature [19,25,67]. Therefore, the chemical starting condition for decomposition events of α' in this work (or more general in case of Ti-6Al-4V α+α' microstructures) is different from that proposed in the literature on the fully-martensitic case cited just above. Moreover, the α'-plates are much finer in the case of dual-phase α+α' microstructures, as their morphology is governed by the prior-β grain size (compare for example [22] to [68]).

However, it can be stated that in all cases the supply of thermal energy causes β-stabilizers to be expelled from the original martensitic regions, which are supersaturated with these elements. Interfaces consistently play a crucial role, serving as early segregation sites for β-stabilizers during the initial martensitic decomposition and acting as preferred nucleation sites for the progressive formation of the β-phase during decomposition. The results of C. Liu et al. [63] further suggest that similar mechanisms are active in the martensitic decomposition processes of other titanium-based alloy systems. The segregation behavior and diffusion kinetics of alloying elements likely have a strong impact on the decomposition in case of both fully martensitic and dual-phase α+α' microstructures. In α+α' microstructures, elemental partitioning between α and β prior to quenching, or, in other words, the

degree of α'-supersaturation, is assumed to be another decisive factor governing the thermodynamic driving force and kinetic pathways of α'-decomposition. Moreover, the interface density - and thus the fineness of α'-plates and nano-twins within α'-plates - may affect the kinetics of β-nucleation and subsequent chemical redistribution, as well as the potential localization of the newly formed β-phase.

4.3. Correlation between microstructure and mechanical properties of different material states

In the following, the microstructural evolution induced by the applied short-time heat treatments is correlated with the resulting mechanical properties of Ti-6Al-4V.

Firstly, as interstitial oxygen is known to can influence the strength of titanium alloys [69,70], its potential contribution is briefly considered. Oxygen measurements for the AR, STQ, and STA1 conditions show only a minor increase along the applied heat treatment route (see Supplementary Note 5). This limited change is attributed to the short heat treatment durations as well as the argon atmosphere used during heat treatments. Further considering the diffusion-controlled oxygen uptake from the surface toward the material interior [71,72], the bulk oxygen content can be assumed comparable, and its influence on the mechanical properties is therefore considered subordinate to the effects of the microstructural evolution discussed below.

As the microstructure of the AR-state consists primarily of the α-phase, deformation can be assumed to be governed by α-phase properties, the α_p grain size (Hall-Petch effect), and α/α grain boundaries, as discussed in [25]. The stress-strain curve shows a distinct yield point (Fig. 11 b)), likely due to interstitial solute atoms impeding dislocation movement, followed by sudden dislocation release.

In contrast to the AR-state, the STQ-state (915 °C, 120 s, WQ) exhibits a significantly lower YS but higher WHR, UEL, and ELF. As shown in literature, α'-martensite has a lower yield strength and hardness than α_p, and deformation is initiated in it despite the potential strengthening effect provided by multiple α'/α' interfaces [23,73]. This suggests that the Hall-Petch effect within β_{trans}-structures is not offsetting the lower yield strength related to the different chemical composition and the RIP-effect. The macroscopic deformation is governed by the chemical and mechanical differences between α_p and α', as well as their deformation compatibility. As a result, the dual-phase STQ-α+α' microstructure behaves like a composite. More specifically, the preferential deformation of the softer α'-martensite-packages (β_{trans}-grains) leads to the formation of geometrically necessary dislocations (GNDs) in the adjacent α_p-grains to accommodate local strain differences. These dislocations increase the dislocation density in the α_p-phase, hindering further dislocation movement and thereby likely contributing to significant work-hardening of the material, as described in Refs. [22,24].

In the STA1-state, the fine structure of the β_{trans} microstructure, or more precisely of the former α'-plates, is retained. Nevertheless, STA1 shows a higher β_{trans} hardness compared to the STQ-state (see [25]) and is characterized by significantly increased tensile strengths (see Fig. 11 a)). Even compared to the AR-state, the STA1-state shows a significantly increased strength. We hypothesize that suppression of the RIP mechanism, as described by O. Dumas et al. [41], already occurs at this early stage of martensite decomposition in the STA1-state. The presence of V-/Fe-enriched clusters and first bcc-precipitates may alter the interfacial configuration sufficiently to inhibit RIP. Moreover, it is plausible that these clusters/first bcc-β-precipitates and/or other solute elements may interact with dislocations, thereby contributing to the strengthening effect. In addition, the relaxation of the martensitic lattice may further impede the RIP mechanism by modifying the state of the original α'/α' interfaces.

Between the annealed STA1 and STA6 conditions, the differences in the work-hardening behavior and yielding nature suggest that the interaction between dislocations and solute atoms undergoes a change with increasing annealing time. It is plausible that the transition from rather isolated solute atoms to solute clusters leads to distinct interaction patterns. While classical solid solution friction is likely after a short annealing time, after a prolonged one, dislocations are likely to be initially pinned by solute clusters until they overcome the pinning and interact with them during further deformation. In this context, the time available for solute diffusion and redistribution appears to be the decisive parameter, as it governs the segregation of solutes to lattice defects and interfaces, thereby affecting yielding behavior and work-hardening. Additionally, the slight coarsening of the β_{trans} microstructure with increasing annealing time (Hall-Petch correlation), as well as the reduction in phase strains and increasing recovery processes of dislocations with increasing annealing time can be made partially reasonable for the reduction in strength. Considering that prolonged annealing would be expected to promote further oxygen uptake, the observed decrease in strength with increasing annealing time further supports the assumption outlined above that the strength evolution is primarily governed by microstructural changes, while slight variations in the oxygen content play only a minor role.

A comparison of the microstructure of the STA6-state with that of the AR-state reveals similar phase fractions and only slight differences in the phase microstrains of α and β. However, the morphology and arrangement of the phases differs significantly. The AR microstructure is characterized by α-grains in the median area size range of $A_{50\%} = 18.6\ \mu m^2$ [25] with only ~3.9 (this work) - 4.5 % ([25]) β-phase located at the grain boundaries of the α-grains. In contrast, the STA6 microstructure consists of α_p - comparable to the α-phase of the AR state - next to significantly finer "lamellar" α-structures that have developed from the preceding STQ-β_{trans} microstructure. The finer α-lamellae show a higher aspect ratio than the primary α-grains and are enveloped by thin, discontinuous β-films. Such β-films also manifest at the former twin boundaries within the former α'-lamellae. It is evident that the enhanced strength of STA6 compared to AR can be mainly attributed to the substantially finer average α-grain size, i.e., via the Hall-Petch correlation. However, an influence of slight differences in phase strain and lattice parameters between the two materials cannot be entirely excluded.

Fracture surface analyses revealed predominantly ductile fracture with a dimpled morphology for all investigated conditions, including the STA-states. As no distinct features enabling a clear correlation with specific microstructural components were observed, representative fracture surfaces are provided in the Supplementary Note 6.

Overall, the results demonstrate that the properties of Ti-6Al-4V are susceptible to substantial modification by adjusting different metastable and stable modifications within the microstructure. In particular, it should be emphasized that the strength of Ti-6Al-4V α+α' microstructures can be significantly increased by additional annealing, whereby the annealing time can be used as a further tuning screw for setting the mechanical properties. Since the underlying decomposition process is partially controlled by the diffusion behavior of the alloying elements, it can be hypothesized that in addition to the annealing time, the annealing temperature also plays a decisive role due to the influence on thermal activation. Furthermore, we would like to emphasize that the potential to induce analogous property alterations through this approach of martensite decomposition is expected to be also applicable to some other titanium-based alloys that allow martensitic transformation.

4.4. New insights and contextualization

In the previous own work by N. Pfeffer et al. [25], a noticeable increase in strength after short-time annealing of α+α'-Ti-6Al-4V microstructures has been reported. However, the explanation was limited to a largely phenomenological and constituent-level description. The present study now provides direct evidence for the early stages of martensite decomposition. The combined HRSTEM, APT, and HEXRD approaches allowed the relevant nanoscale mechanisms to be resolved. The onset of the α' → α+β transformation reveals a sequence of processes, including

(i) segregation of β-stabilizers to interfaces, (ii) the transition from V-/(Fe-)rich interfacial layers or enrichments to discrete V-/Fe-enriched clusters and/or first β-nuclei, (iii) concurrent crystallographic relaxation of the former α'-phase, together with an increased geometrical complexity of α_p/β_{trans} interfaces, consistent with stress-driven interfacial reconfiguration during early martensite decomposition. Moreover, the time-dependency of the martensite decomposition is revealed in both crystallographic and chemical terms: from early segregation and clustering of β-stabilizing elements through progressive elemental redistribution and β-related feature formation to the equilibrium α+β state. In combination with the results reported in [25], this enabled an in-depth understanding of the between the nano-/microstructural changes and the mechanical responses of the STA-states.

An additional question arises in this context: what makes the annealing approach in this work so special compared to those applied to LPBF and fully martensitic Ti-6Al-4V microstructures? The dual-phase α+α' microstructures in our case represent a fundamentally different starting condition for martensite decomposition induced by annealing. The two constituents, α and α', are chemically, crystallographically, and morphologically distinct, and additional α_p/β_{trans} interfaces are present. The results of this work show that martensite decomposition in such microstructures is governed by a coupled set of chemical, crystallographic, and deformation-related processes, with additional contributions compared to fully martensitic states. In particular, the suppression of reorientation-induced plasticity, which is characteristic of dual-phase α+α' Ti-6Al-4V microstructures, constitutes an additional strengthening pathway that is absent in fully martensitic states.

Overall, the present study provides a mechanism-based understanding of the strength increase during (short-time) annealing in dual-phase α+α' Ti-6Al-4V and its coupling to the mechanical response during progressive decomposition.

5. Conclusion

This study provides in-depth insights into the α'-martensite decomposition during annealing of Ti-6Al-4V with an initial dual-phase α+α' microstructure, with the latter produced by short-time solution heat treatment of the AR-material at 915 °C followed by water-quenching. Crystallographic evolution and concurrent chemical changes during the α' → α+β transformation were identified through detailed analysis, revealing mechanisms that potentially contribute to strengthening. The following conclusions can be drawn:

- The α+α' microstructure consists of approximately equal fractions of primary α (α_p) and transformed β (β_{trans}), with α'-martensite appearing as a fine plate-like transformation product. Compared to the α_p- and α_{eq}-phases, α' is enriched and even supersaturated in β-stabilizers V and Fe. Further it is characterized by a high distortion energy, since the lattice correspondence with the bcc parent phase forces it into a distorted hcp structure. Mechanically, the α+α'-state exhibits a comparatively low yield strength (~839 MPa), pronounced work hardening, and good ductility.
- **Short-time annealing (570 °C, 180 s):** V-/Fe-segregation to α_p/β_{trans} and α'/α' interfaces as well as to transformation twin interfaces within α' led to the formation of V-/Fe-rich nano-scale clusters. These chemical changes occurred concurrently with crystallographic martensite decomposition. Consequently, the original distorted hcp lattice of the α'-phase underwent a relaxation, with a c/a ratio approaching the equilibrium value of the hcp α-phase. Segregated regions partially exhibited a bcc structure (~1.1 %).
- **Prolonged annealing:** the β_{trans}-microstructure progressively transformed towards the equilibrium α+β structure. Accordingly, β precipitation progressed, as evidenced by an increasing β-phase fraction. Its occurrence along interfaces strongly suggests that it evolved from V-/Fe-rich clusters and β-nuclei. Further, migration of the α_p/β_{trans} interface into the direction of former martensitic regions was evident. Continuous lattice parameter changes indicated ongoing elemental partitioning between α and β, accompanied by ongoing lattice relaxation of both phases. After 3 h of annealing, the microstructure approached a saturated state, and at longer times lattice parameters and phase fractions remained essentially unchanged. This, together with comparison to the as-received material, strongly suggested that a near-equilibrium condition had been reached. After 6 h, the β-phase fraction amounted to ~4.2 %.
- **Mechanical properties**: The stage of α' → α+β transformation strongly influenced the mechanical response. Stress-strain curves indicated that the reorientation-induced plasticity effect, characteristic of Ti-6Al-4V α+α' microstructures, is suppressed already after short-time annealing, and likely contributes to the observed significant strength increase (yield strength: ~1111 MPa) respective to the initial α+α' microstructure. Additionally, fine V-/Fe-rich clusters and first β-precipitates may have further enhanced strengthening. The strength and work-hardening were found to decrease with increasing annealing time and this was attributed to changes in dislocation-solute interactions as well as microstructural coarsening, including an increase in α-lamellae size.

Due to the diffusion-controlled nature of the observed processes during annealing, the annealing temperature is expected to strongly influence microstructural and mechanical evolution. Similar microstructural changes to those reported here for Ti-6Al-4V are expected to also occur during annealing of other titanium alloys exhibiting α+α' or α+α'' microstructures, although the kinetics are likely dependent on the specific alloying elements.

CRediT authorship contribution statement

N. Pfeffer: Writing – review & editing, Writing – original draft, Visualization, Validation, Methodology, Investigation, Formal analysis, Data curation, Conceptualization. **A. Bezold:** Writing – review & editing, Methodology, Investigation, Formal analysis. **J. Vollhüter:** Methodology, Investigation, Formal analysis. **O. Nagel:** Methodology, Investigation, Formal analysis. **M. Weiser:** Methodology. **A. Stark:** Methodology, Investigation. **S. Neumeier:** Writing – review & editing, Resources. **H.W. Höppel:** Writing – review & editing, Supervision, Resources, Project administration, Funding acquisition, Conceptualization.

Funding

This work was supported by the German Federal Ministry for Economic Affairs and Energy (BMWE) as part of the joint research project TISTRAQ (funding reference: 20Q1927C). Project partners of Institute I of FAU within this project are HEGGEMANN AG and DYNAmore GmbH, an Ansys company.

Declaration of competing interest

The authors declare that they have no known competing financial interests or personal relationships that could have appeared to influence the work reported in this paper.

Acknowledgments

The authors would like to acknowledge Deutsches Elektronen Synchrotron, DESY (Hamburg, Germany), a member of the Helmholtz Association HGF, for the provision of experimental facilities at PETRA III/P07-High Energy Materials (HEMA) beamline (proposal: I-20230881). AB gratefully acknowledges financial support from the Alexander-von-Humboldt Foundation.

Appendix A. Supplementary data

Supplementary data to this article can be found online at https://doi.org/10.1016/j.msea.2026.150024.

Data availability

Data will be made available on request.

References

[1] G. Lütjering, Property optimization through microstructural control in titanium and aluminum alloys, Mater. Sci. Eng., A 263 (1999) 117–126, https://doi.org/10.1016/S0921-5093(98)01169-1.

[2] S.A. Mantri, D. Choudhuri, T. Alam, G.B. Viswanathan, J.M. Sosa, H.L. Fraser, R. Banerjee, Tuning the scale of α precipitates in β-titanium alloys for achieving high strength, Scr. Mater. 154 (2018) 139–144, https://doi.org/10.1016/j.scriptamat.2018.05.040.

[3] C. Zhang, J. Zhang, X. Bao, J. Li, D. Zhang, G. Liu, J. Sun, Hierarchically ordered coherent interfaces-driven ultrahigh specific-strength and toughness in a nano-martensite titanium alloy, Acta Mater. 263 (2024) 119540, https://doi.org/10.1016/j.actamat.2023.119540.

[4] C. Zhang, X. Bao, M. Hao, W. Chen, D. Zhang, D. Wang, J. Zhang, G. Liu, J. Sun, Hierarchical nano-martensite-engineered a low-cost ultra-strong and ductile titanium alloy, Nat. Commun. 13 (2022) 5966, https://doi.org/10.1038/s41467-022-33710-1.

[5] Z. Tarzimoghadam, S. Sandlöbes, K.G. Pradeep, D. Raabe, Microstructure design and mechanical properties in a near-α Ti–4Mo alloy, Acta Mater. 97 (2015) 291–304, https://doi.org/10.1016/j.actamat.2015.06.043.

[6] H. Zhang, J. Zhang, S. Liu, D. Zhang, G. Liu, J. Sun, Designing ultra-strong and ductile hierarchical titanium alloys via interstitial solute-mediated multi-morphologic α-nanoprecipitates, Acta Mater. 255 (2023) 119082, https://doi.org/10.1016/j.actamat.2023.119082.

[7] G. Lütjering, Influence of processing on microstructure and mechanical properties of (α+β) titanium alloys, Mater. Sci. Eng., A 243 (1998) 32–45, https://doi.org/10.1016/S0921-5093(97)00778-8.

[8] S.L. Semiatin, An overview of the thermomechanical processing of α/β titanium alloys: current status and future research opportunities, Metall. Mater. Trans. A 51 (2020) 2593–2625, https://doi.org/10.1007/s11661-020-05625-3.

[9] W.G. Burgers, On the process of transition of the cubic-body-centered modification into the hexagonal-close-packed modification of zirconium, Physica 1 (1934) 561–586, https://doi.org/10.1016/S0031-8914(34)80244-3.

[10] J.B. Newkirk, A.H. Geisler, Crystallographic aspects of the beta to alpha transformation in titanium, Acta Metall. 1 (1953) 370–374, https://doi.org/10.1016/0001-6160(53)90113-8.

[11] A.J. Williams, R.W. Cahn, C.S. Barrett, The crystallography of the β-α transformation in titanium, Acta Metall. 2 (1954) 117–128, https://doi.org/10.1016/0001-6160(54)90101-7.

[12] E.G. Brock, Field emission microscopy of an allotropic transformation: α − β titanium, Phys. Rev. 100 (1955) 1619–1626, https://doi.org/10.1103/PhysRev.100.1619.

[13] R. Filip, K. Kubiak, W. Ziaja, J. Sieniawski, The effect of microstructure on the mechanical properties of two-phase titanium alloys, J. Mater. Process. Technol. 133 (2003) 84–89, https://doi.org/10.1016/S0924-0136(02)00248-0.

[14] U. Zwicker, Titan Und Titanlegierungen, Softcover Reprint of the Hardcover, first ed., Springer, Berlin Heidelberg New York, 2014.

[15] H.H. Weigand, Zur Umwandlung von α+β - titanlegierungen mit Aluminium, Int. J. Mater. Res. 54 (1963) 43–49, https://doi.org/10.1515/ijmr-1963-540109.

[16] T. Ahmed, H.J. Rack, Phase transformations during cooling in α+β titanium alloys, Mater. Sci. Eng., A 243 (1998) 206–211, https://doi.org/10.1016/S0921-5093(97)00802-2.

[17] R. Dąbrowski, The kinetics of phase transformations during continuous cooling of the Ti6Al4V alloy from the single-phase ß range, Arch. Metall. Mater. 56 (2011) 703–707, https://doi.org/10.2478/v10172-011-0077-x.

[18] H.M. Flower, R. Davis, D.R.F. West, Martensite formation and decomposition in alloys of titanium containing β-stabilizing elements, in: J.C. Williams, A.F. Belov (Eds.), Titanium and Titanium Alloys, Springer US, Boston, MA, 1982, pp. 1703–1715, https://doi.org/10.1007/978-1-4757-1758-7_8.

[19] Y.T. Lee, M. Peters, G. Welsch, Elastic moduli and tensile and physical properties of heat-treated and quenched powder metallurgical Ti-6Al-4V alloy, Metall. Trans. A 22 (1991) 709–714, https://doi.org/10.1007/BF02670293.

[20] O. Dumas, L. Malet, P. Kwaśniak, F. Prima, S. Godet, Design rules to develop solute lean α+β titanium alloys exhibiting high work-hardening by reorientation induced plasticity, Mater. Sci. Eng., A 890 (2024) 145935, https://doi.org/10.1016/j.msea.2023.145935.

[21] O. Dumas, L. Malet, P. Kwaśniak, F. Prima, S. Godet, Reorientation induced plasticity (RIP) in high-strength titanium alloys: an insight into the underlying mechanisms and resulting mechanical properties, Acta Mater. 246 (2023) 118679, https://doi.org/10.1016/j.actamat.2023.118679.

[22] Y. Chong, T. Bhattacharjee, Y. Tian, A. Shibata, N. Tsuji, Deformation mechanism of bimodal microstructure in Ti-6Al-4V alloy: the effects of intercritical annealing temperature and constituent hardness, J. Mater. Sci. Technol. 71 (2021) 138–151, https://doi.org/10.1016/j.jmst.2020.08.057.

[23] Y. Chong, T. Bhattacharjee, M.-H. Park, A. Shibata, N. Tsuji, Factors determining room temperature mechanical properties of bimodal microstructures in Ti-6Al-4V alloy, Mater. Sci. Eng., A 730 (2018) 217–222, https://doi.org/10.1016/j.msea.2018.06.019.

[24] C. de Formanoir, A. Brulard, S. Vivès, G. Martin, F. Prima, S. Michotte, E. Rivière, A. Dolimont, S. Godet, A strategy to improve the work-hardening behavior of Ti–6Al–4V parts produced by additive manufacturing, Mater. Res. Lett. 5 (2017) 201–208, https://doi.org/10.1080/21663831.2016.1245681.

[25] N. Pfeffer, S.N. Jäger, M.A. Kaiser, T. Meyer, A. Stark, H.W. Höppel, Enhancing mechanical strength of Ti-6Al-4V sheet material by short-time sub-β-transus solution heat treatment and additional short-time annealing, Mater. Sci. Eng. A (2025) 147787, https://doi.org/10.1016/j.msea.2025.147787.

[26] O. Dumas, L. Malet, B. Hary, F. Prima, S. Godet, Crystallography and reorientation mechanism upon deformation in the martensite of an α-α' Ti-6Al-4V dual-phase microstructure exhibiting high work-hardening rate, Acta Mater. 205 (2021) 116530, https://doi.org/10.1016/j.actamat.2020.116530.

[27] O. Dumas, B. Hary, G. Martin, F. Sun, C. de Formanoir, F. Prima, S. Godet, Towards work-hardenability of Ti-6Al-4V through a quenching and partitioning approach, MATEC Web Conf. 321 (2020) 11062, https://doi.org/10.1051/matecconf/202032111062.

[28] N. Pfeffer, M.A. Kaiser, W. Feix, N. Kälble, M. Merten, A. Stark, A. Haufe, T. Meyer, T. Tröster, H.W. Höppel, Energy- and material-efficient Ti-6Al-4V sheet part fabrication by the novel TISTRAQ-process, including resistance heating and tool-based quenching: insights into test stand design and material potential, Mater. Sci. Eng. A (2025) 149015, https://doi.org/10.1016/j.msea.2025.149015.

[29] T. Morita, K. Hatsuoka, T. Iizuka, K. Kawasaki, Strengthening of Ti-6Al-4V alloy by short-time duplex heat treatment, Mater. Trans. 46 (2005) 1681–1686, https://doi.org/10.2320/matertrans.46.1681.

[30] S. Tanaka, T. Morita, K. Shinoda, Effects of short-time duplex heat treatment on microstructure and fatigue strength of Ti-6Al-4V alloy, in: Proceedings of the 13th International Conference on Fracture, 2013.

[31] P.J. Fopiano, C.F. Hickey Jr., A. Materials, M.R.C.W. Ma, Strengthening Mechanisms During the Heat Treatment of Three Titanium Alloys - Ti-6Al-4V, Ti-6Al-6V-2Sn, and Ti-8Al-1Mo-1V, CFSTI, 1968.

[32] M.V. Pantawane, S. Dasari, S.A. Mantri, R. Banerjee, N.B. Dahotre, Rapid thermokinetics driven nanoscale vanadium clustering within martensite laths in laser powder bed fused additively manufactured Ti6Al4V, Mater. Res. Lett. 8 (2020) 383–389, https://doi.org/10.1080/21663831.2020.1772396.

[33] J. Haubrich, J. Gussone, P. Barriobero-Vila, P. Kürnsteiner, E.A. Jägle, D. Raabe, N. Schell, G. Requena, The role of lattice defects, element partitioning and intrinsic heat effects on the microstructure in selective laser melted Ti-6Al-4V, Acta Mater. 167 (2019) 136–148, https://doi.org/10.1016/j.actamat.2019.01.039.

[34] H. Wang, Q. Chao, H.S. Chen, Z.B. Chen, S. Primig, W. Xu, S.P. Ringer, X.Z. Liao, Formation of a transition V-rich structure during the α' to α + β phase transformation process in additively manufactured Ti-6Al-4V, Acta Mater. 235 (2022) 118104, https://doi.org/10.1016/j.actamat.2022.118104.

[35] G.M. Ter Haar, T.H. Becker, Low temperature stress relief and martensitic decomposition in selective laser melting produced Ti6Al4V, Mater. Des. Process. Commun. 3 (2021), https://doi.org/10.1002/mdp2.138.

[36] Q. Gaillard, X. Boulnat, S. Cazottes, S. Dancette, C. Desrayaud, Strength/ductility trade-off of laser powder bed fusion Ti-6Al-4V: synergetic effect of alpha-case formation and microstructure evolution upon heat treatments, Addit. Manuf. 76 (2023) 103772, https://doi.org/10.1016/j.addma.2023.103772.

[37] S. Cao, R. Chu, X. Zhou, K. Yang, Q. Jia, C.V.S. Lim, A. Huang, X. Wu, Role of martensite decomposition in tensile properties of selective laser melted Ti-6Al-4V, J. Alloys Compd. 744 (2018) 357–363, https://doi.org/10.1016/j.jallcom.2018.02.111.

[38] W. Xu, M. Brandt, S. Sun, J. Elambasseril, Q. Liu, K. Latham, K. Xia, M. Qian, Additive manufacturing of strong and ductile Ti–6Al–4V by selective laser melting via in situ martensite decomposition, Acta Mater. 85 (2015) 74–84, https://doi.org/10.1016/j.actamat.2014.11.028.

[39] X.-Y. Zhang, G. Fang, S. Leeflang, A.J. Böttger, A.A. Zadpoor, J. Zhou, Effect of subtransus heat treatment on the microstructure and mechanical properties of additively manufactured Ti-6Al-4V alloy, J. Alloys Compd. 735 (2018) 1562–1575, https://doi.org/10.1016/j.jallcom.2017.11.263.

[40] J. Su, X. Ji, J. Liu, J. Teng, F. Jiang, D. Fu, H. Zhang, Revealing the decomposition mechanisms of dislocations and metastable α' phase and their effects on mechanical properties in a Ti-6Al-4V alloy, J. Mater. Sci. Technol. 107 (2022) 136–148, https://doi.org/10.1016/j.jmst.2021.07.048.

[41] O. Dumas, L. Malet, G. Martin, P. Kwasniak, F. Prima, S. Godet, Exploring the strength-ductility space of Ti-6Al-4V through a quenching and partitioning approach, Mater. Sci. Eng., A 925 (2025) 147859, https://doi.org/10.1016/j.msea.2025.147859.

[42] H. Kellerer, Übersicht über die Wärmebehandlung von TiAl6V4, HTM J. Heat Treatm, Materials 25 (1970) 242–253, https://doi.org/10.1515/htm-1970-250404.

[43] K. Thompson, D. Lawrence, D.J. Larson, J.D. Olson, T.F. Kelly, B. Gorman, In situ site-specific specimen preparation for atom probe tomography, Ultramicroscopy 107 (2007) 131–139, https://doi.org/10.1016/j.ultramic.2006.06.008.

[44] M.K. Miller, K.F. Russell, K. Thompson, R. Alvis, D.J. Larson, Review of atom probe FIB-based specimen preparation methods, Microsc. Microanal. 13 (2007) 428–436, https://doi.org/10.1017/S1431927607070845.

[45] N. Schell, R.V. Martins, F. Beckmann, H.U. Ruhnau, R. Kiehn, A. Schreyer, The high energy materials science beamline at PETRA III, MS 571–572 (2008) 261–266. https://doi.org/10.4028/www.scientific.net/MSF.571-572.261.

[46] M. Storm, G. Lotze, Pydidas - Python Diffraction Data Analysis Suite, 2025, https://doi.org/10.5281/ZENODO.7568610.
[47] J. Rodríguez-Carvajal, Recent advances in magnetic structure determination by neutron powder diffraction, Phys. B Condens. Matter 192 (1993) 55–69, https://doi.org/10.1016/0921-4526(93)90108-I.
[48] W.A. Dollase, Correction of intensities for preferred orientation in powder diffractometry: application of the march model, J. Appl. Crystallogr. 19 (1986) 267–272, https://doi.org/10.1107/S0021889886089458.
[49] G. Lindwall, K.-W. Moon, Z. Chen, M. Mengason, M.E. Williams, J.M. Gorham, J.-C. Zhao, C.E. Campbell, Diffusion in the Ti-Al-V system, J. Phase Equilibria Diffus. 39 (2018) 731–746, https://doi.org/10.1007/s11669-018-0673-9.
[50] G.K. Williamson, W.H. Hall, X-ray line broadening from filed aluminium and wolfram, Acta Metall. 1 (1953) 22–31, https://doi.org/10.1016/0001-6160(53)90006-6.
[51] H.T. Clark, The lattice parameters of high purity alpha titanium; and the effects of oxygen and nitrogen on them, JOM 1 (1949) 588–589, https://doi.org/10.1007/BF03398899.
[52] R. Boyer, G. Welsch, E.W. Collings (Eds.), Materials Properties Handbook: Titanium Alloys, 4. Printing, ASM International, Materials Park, Ohio, 2007.
[53] G. Aurelio, A.F. Guillermet, Assessment of the structural relations between the bcc and omega phases of Ti, Zr, Hf and other transition metals, Int. J. Mater. Res. 91 (2000) 35–42, https://doi.org/10.1515/ijmr-2000-910110.
[54] F.R. Kaschel, R.K. Vijayaraghavan, A. Shmeliov, E.K. McCarthy, M. Canavan, P. J. McNally, D.P. Dowling, V. Nicolosi, M. Celikin, Mechanism of stress relaxation and phase transformation in additively manufactured Ti-6Al-4V via in situ high temperature XRD and TEM analyses, Acta Mater. 188 (2020) 720–732, https://doi.org/10.1016/j.actamat.2020.02.056.
[55] S.A. Oh, J.W. Aroh, N.L. Lamprinakos, C.A. Chuang, A.N. Bucsek, A.D. Rollett, Martensite decomposition during rapid heating of Ti-6Al-4V studied via in situ synchrotron X-ray diffraction, Commun. Mater. 5 (2024) 58, https://doi.org/10.1038/s43246-024-00492-6.
[56] M. Bignon, E. Bertrand, P.E.J. Rivera-Díaz-del-Castillo, F. Tancret, Martensite formation in titanium alloys: crystallographic and compositional effects, J. Alloys Compd. 872 (2021) 159636, https://doi.org/10.1016/j.jallcom.2021.159636.
[57] A.V. Dobromyslov, V.A. Elkin, The orthorhombic α″-phase in binary titanium-base alloys with d-metals of V–VIII groups, mater, Sci. Eng. A 438–440 (2006) 324–326, https://doi.org/10.1016/j.msea.2006.02.086.
[58] W. Rostoker, Observations on the lattice parameters of the alpha solid solution in the titanium-aluminum system, JOM 4 (1952) 212–213, https://doi.org/10.1007/BF03397677.
[59] P. Mwangi, A. Otsu, Z.-C. Chen, First-principles calculations on the effect of interstitial oxygen on structural, thermodynamic, and elastic properties of titanium-oxygen alloys, Comput. Mater. Sci. 246 (2025) 113405, https://doi.org/10.1016/j.commatsci.2024.113405.
[60] L. -c. Ming, M.H. Manghnani, K.W. Katahara, Phase transformations in the Ti-V system under high pressure up to 25 GPa, Acta Metall. 29 (1981) 479–485, https://doi.org/10.1016/0001-6160(81)90071-7.
[61] J.L. Murray, The ti−v (Titanium-Vanadium) system, Bull. Alloy Phase Diagr. 2 (1981) 48–55, https://doi.org/10.1007/BF02873703.
[62] J.C. Williams, R. Taggart, D.H. Polonis, The morphology and substructure of Ti-Cu martensite, Metall. Trans. A 1 (1970) 2265–2270, https://doi.org/10.1007/BF02643444.
[63] C. Liu, X. Hu, L. Qi, H. Chen, Z. Li, X. Zhang, H. Yan, K. Zhou, M. Song, Y. Wang, J.-F. Nie, Unusual precipitation induced by solute segregation in coherent twin boundary in titanium alloys, Acta Mater. 242 (2023) 118466, https://doi.org/10.1016/j.actamat.2022.118466.
[64] T. Voisin, N.P. Calta, S.A. Khairallah, J.-B. Forien, L. Balogh, R.W. Cunningham, A. D. Rollett, Y.M. Wang, Defects-dictated tensile properties of selective laser melted Ti-6Al-4V, Mater. Des. 158 (2018) 113–126, https://doi.org/10.1016/j.matdes.2018.08.004.
[65] D. Wen, V. Tucker, M.S. Titus, A layer model for the kinetics of segregation in planar defects in multi-component materials, Acta Mater. 290 (2025) 120948, https://doi.org/10.1016/j.actamat.2025.120948.
[66] R.A. Fournelle, J.B. Clark, The genesis of the cellular precipitation reaction, Metall. Trans. A 3 (1972) 2757–2767, https://doi.org/10.1007/BF02652842.
[67] S. Huang, J. Zhang, Y. Ma, S. Zhang, S.S. Youssef, M. Qi, H. Wang, J. Qiu, D. Xu, J. Lei, R. Yang, Influence of thermal treatment on element partitioning in α+β titanium alloy, J. Alloys Compd. 791 (2019) 575–585, https://doi.org/10.1016/j.jallcom.2019.03.332.
[68] Y. Chong, T. Bhattacharjee, J. Yi, A. Shibata, N. Tsuji, Mechanical properties of fully martensite microstructure in Ti-6Al-4V alloy transformed from refined beta grains obtained by rapid heat treatment (RHT), Scr. Mater. 138 (2017) 66–70, https://doi.org/10.1016/j.scriptamat.2017.05.038.
[69] J.-M. Oh, B.-G. Lee, S.-W. Cho, S.-W. Lee, G.-S. Choi, J.-W. Lim, Oxygen effects on the mechanical properties and lattice strain of Ti and Ti-6Al-4V, Met. Mater. Int. 17 (2011) 733–736, https://doi.org/10.1007/s12540-011-1006-2.
[70] Y. Song, G. Wang, Y. Zhang, M. Zhu, S. Xie, H. Kou, Mechanism of trace oxygen promoting ductility in as-cast Ti-6Al-4V alloys, Mater. Sci. Eng., A 930 (2025) 148176, https://doi.org/10.1016/j.msea.2025.148176.
[71] H. Fukai, H. Iizumi, K. Minakawa, C. Ouchi, The effects of the oxygen-enriched surface layer on mechanical properties of α+β type titanium alloys, ISIJ Int. 45 (2005) 133–141, https://doi.org/10.2355/isijinternational.45.133.
[72] H. Fei, B. Pan, C. Zhang, Y. Jiang, Q. Xu, Y. Lu, J. Gong, Study on the mechanical properties gradient in surface oxygen diffusion hardened layer of Ti6Al4V alloy, J. Mater. Res. Technol. 18 (2022) 3173–3183, https://doi.org/10.1016/j.jmrt.2022.04.028.
[73] C. de Formanoir, G. Martin, F. Prima, S.Y.P. Allain, T. Dessolier, F. Sun, S. Vivès, B. Hary, Y. Bréchet, S. Godet, Micromechanical behavior and thermal stability of a dual-phase α+α' titanium alloy produced by additive manufacturing, Acta Mater. 162 (2019) 149–162, https://doi.org/10.1016/j.actamat.2018.09.050.